Exciton states and optical properties of carbon nanotubes

2012 J. Phys.: Condens. Matter 24 483001

(http://iopscience.iop.org/0953-8984/24/48/483001)

IOP PUBLISHING JOURNAL OF PHYSICS: CONDENSED MATTER

J. Phys.: Condens. Matter **24** (2012) 483001 (25pp) doi:10.1088/0953-8984/24/48/483001

TOPICAL REVIEW

Exciton states and optical properties of carbon nanotubes

Hiroshi Ajiki

Photon Pioneers Center, Osaka University, 2-8 Yamadaoka, Suita, Osaka 565-0871, Japan

E-mail: ajiki@ppc.osaka-u.ac.jp

Received 21 February 2012
Published 9 November 2012
Online at stacks.iop.org/JPhysCM/24/483001

Abstract
Exciton states and related optical properties of a single-walled carbon nanotube are reviewed, primarily from a theoretical viewpoint. The energies and wavefunctions of excitons are discussed using a screened Hartree–Fock approximation with an effective-mass or $\boldsymbol{k}\cdot\boldsymbol{p}$ approximation. The close relationship between a long-range electron–hole exchange interaction and a depolarization effect is clarified. I discuss optical properties including the radiative lifetime of excitons, absorption spectra and radiation force. To describe these properties in a unified scheme, a self-consistent method is introduced for calculating the scattering light and induced current density due to excitons. I also briefly review experimental results on the Aharonov–Bohm effect in excitons and quasi-dark excitons excited by light polarized perpendicular to the tube axis.

(Some figures may appear in colour only in the online journal)

Contents

1. Introduction

Carbon nanotubes have the structure of a seamlessly rolled-up graphite sheet or graphene. They were discovered by Iijima in 1991, and their crystal structure was determined from the electron diffraction patterns [1] (similar carbon fibers were reported by Endo [2]). These nanotubes, which are called multi-walled nanotubes, consist of a few concentric tubes, each of which has carbon-atom hexagons arranged chirally about the axis. After the discovery of multi-walled nanotubes, single-walled carbon nanotubes (SWNTs) were produced intentionally [3, 4]. The purpose of this paper is to provide a brief review of the exciton states and optical properties of a SWNT.

A SWNT has very attractive properties because of its cylindrical quasi-one-dimensional (quasi-1D) structure. For example, depending on its diameter and chirality, a SWNT can be a metal or a semiconductor whose bandgap is inversely proportional to the diameter [5–9]. In addition, the bandgap can be changed using the Aharonov–Bohm (AB) effect by applying a magnetic flux that passes through the tube axis [10]. These fascinating properties of the bandgap can be observed directly by optical spectroscopy.

Optical spectra are understood simply in terms of band-to-band transitions. This simple picture successfully describes the overall trends in the relationship between the transition energies and structures of SWNTs. In fact, the chiral index of an individual SWNT has been determined experimentally from the simple band-to-band model [11–13]. In addition, this picture can explain a strong anisotropy of the absorption intensity with respect to the polarization. Although well-defined spectral peaks appear when the polarization is parallel to the tube axis, they are significantly suppressed for perpendicular polarization because of a large depolarization effect [14]. A strong polarization dependence of Raman scattering [15–17], absorption [18, 19] and photoluminescence (PL) [17] has been observed in SWNTs. This anisotropic optical response is called the antenna effect and can be used to determine the degree of alignment of SWNTs. This effect was also used to measure the magnetic susceptibility anisotropy of SWNTs [20–23]. The magnetic susceptibility $\chi_\parallel$ parallel to the tube axis is larger than the perpendicular susceptibility $\chi_\perp$ [24–26]. Consequently, a magnetic field tends to align the axes of SWNTs in the field direction. By combining the tendency to align with a magnetic field and the antenna effect, the values of $\Delta\chi = \chi_\parallel - \chi_\perp$ for SWNTs were determined using high-field magnetic linear dichroism spectroscopy [20–23]. The above combination was also used to demonstrate the AB effect in SWNTs [27–30].

Before the observation of PL, optical absorption by SWNTs was reported [31–33]. The absorption of early samples exhibited broad peaks attributed to large ensembles of SWNTs, which would typically be bundled into ropes and contain some level of impurities. The spectral broadening was resolved by isolating SWNTs separated from those in the bundle [34]. Isolation was achieved by encapsulating individual SWNTs in a cylindrical micelle. The absorption spectra of the isolated SWNTs showed a series of sharp peaks associated with each transition level of individual SWNTs. Furthermore, sharp PL peaks can be observed from the isolated SWNTs [34]. By combining the sharp absorption and PL signals, we can draw a photoluminescence excitation (PLE) map; the PL intensity is recorded as the excitation wavelength is changed. An intensity peak appears when the excitation energy matches that of an absorption resonance from which relaxation to a PL-emitting transition occurs. The spectral intensities are summarized as a three-dimensional map, in which luminescent intensities are plotted on a gray or color scale as functions of the emission and excitation wavelengths. A PLE map obtained from an ensemble of SWNTs exhibits some spots, each of which represents a specific chiral structure of the SWNTs [11]. Thus, PLE mapping is an important method for identifying the chiral structure. These sharp spectral peaks also enable us to study the excited states of an individual SWNT precisely. In fact, the exciton effect, the AB effect on the bandgap and the existence of a quasi-dark exciton were clearly demonstrated by using these isolated SWNTs.

In another isolation technique, SWNTs suspended between mesa structures [35] or on trench structures [36] are fabricated. The absorption and PL peak energies depend on the dielectric constant surrounding the material. This feature is called an environment effect [37, 38] and it was studied by comparing the PLE signals for micelle-encapsulated SWNTs and air-suspended SWNTs [39]. A theoretical study of environment effects has also been reported [40]. Because the suspended SWNTs are free from a surrounding micelle, it is possible to extract their intrinsic optical properties. For example, the diffusion length of excitons in air-suspended SWNTs has been measured and was found to be significantly longer than that in micelle-encapsulated SWNTs [41].

In this paper, we focus on the exciton states and their optical properties, such as absorption and radiation force, of a SWNT. Another important aspect of optical properties is resonant Raman scattering. I shall not discuss this, but I refer readers to the reviews [42, 43] and books [44, 45] on this topic. The optical properties are one of various aspects of carbon nanotubes, which also include the electronic, magnetic, transport, phonon and mechanical properties. Many reviews and books on these topics have been published [44, 46–58].

In section 2 electronic states of a graphene and a SWNT are discussed using the effective-mass or $\boldsymbol{k}\cdot\boldsymbol{p}$ approximation. Higher-order corrections due to trigonal warping, the finite overlap integral and the curvature are introduced in the $\boldsymbol{k}\cdot\boldsymbol{p}$ scheme. In section 3 selection rules of one-photon excitation are discussed for polarization parallel and perpendicular to the tube axis. In section 4 the exciton states of SWNTs are reviewed. The equations of motion of excitons are derived using the screened Hartree–Fock approximation starting from the many-body Hamiltonian. In addition, the exciton states for parallel and perpendicular polarization are calculated. The electron–hole (e–h) exchange interaction (EXI) arises for perpendicular polarization. Using an e–h EXI with a dynamical factor (dynamical e–h EXI), the correct exciton states can be calculated. In section 5 exciton–photon interaction is reviewed. A current due to excitons is generated by an applied field and the induced current produces an electromagnetic (EM) field. Therefore, the current due to excitons and the EM field should be determined self-consistently. The self-consistent treatment generally provides a small correction to the optical response. However, the radiative lifetime of excitons and scattering force of light can be evaluated using the self-consistent

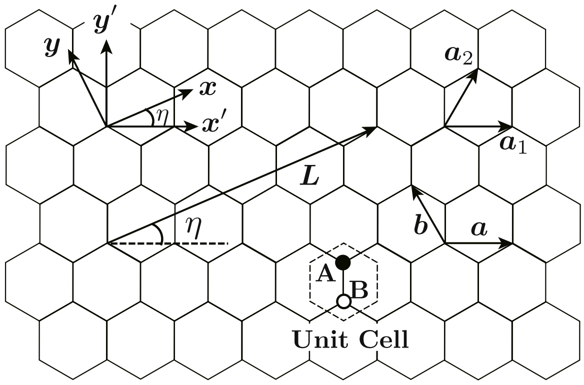

Figure 1. Lattice structure of a graphene and coordinate systems. A and B represent two types of carbon sites in a unit cell. Two primitive translation vectors are denoted by $\boldsymbol{a}$ and $\boldsymbol{b}$. Another choice for the primitive translation vectors is denoted by $\boldsymbol{a}_1$ and $\boldsymbol{a}_2$. The chiral vector and chiral angle of a SWNT are denoted by $\boldsymbol{L}$ and η, respectively. The structure of a SWNT is specified by the chiral vector. $\boldsymbol{x}$ and $\boldsymbol{y}$ are set to the circumferential and axial directions of a SWNT.

treatment. Furthermore, the dynamical e–h EXI can be derived from this treatment. In section 6 optical absorption for parallel and perpendicular polarization is reviewed. The AB effect for SWNTs has been demonstrated in optical spectra. For perpendicular polarization, a quasi-dark exciton appears because of the asymmetry of the electron and hole bands. These experimental topics are also presented. In section 7 radiation force exerted on a SWNT is discussed. Finally, I summarize this review in section 8.

2. Electronic states

2.1. Effective-mass approximation

2.1.1. Graphene. Because the structure of a SWNT is obtained by rolling up a graphene, the SWNT's electronic states can be derived from those of graphene. The crystal structure of a graphene is shown in figure 1. A unit cell of graphene contains two carbon atoms. Therefore, graphene consists of two sublattices whose respective lattice points are called A and B sites. Primitive translation vectors are denoted by $\boldsymbol{a} = a(1, 0)$ and $\boldsymbol{b} = a(-1/2, \sqrt{3}/2)$ in the $\boldsymbol{x}'$–$\boldsymbol{y}'$ coordinates, where $a = 0.246$ nm is the lattice constant (see figure 1). The first Brillouin zone is shown in the inset of figure 2. The K and K′ points at the corners of the Brillouin zone are given by $\boldsymbol{K} = (2\pi/a)(1/3, 1/\sqrt{3})$ and $\boldsymbol{K}' = (2\pi/a)(2/3, 0)$, respectively.

The wavefunction of the p_z orbital (sp_2 hybridized orbitals) of a carbon atom constitutes a π (σ) orbital in graphene. The amplitude of the π orbital is concentrated out-of-plane, whereas that of the σ orbital lies along the bonds between nearest-neighbor carbon atoms. The π orbital specifies the electronic states near the Fermi energy. Figure 2 shows the π band structure calculated in a nearest-neighbor tight-binding model along the K → Γ → M → K points. The Fermi energy is set to 0. The conduction and valence bands touch at the K and K′ points.

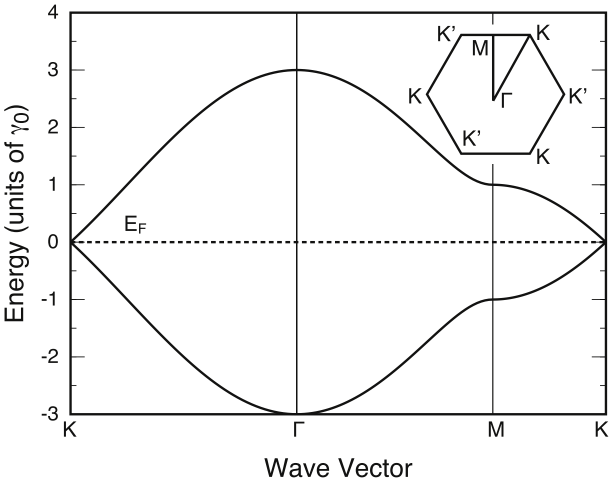

Figure 2. The π band structure of a graphene. Fermi energy lies at $\varepsilon = 0$. The Brillouin zone and high symmetry points K, K′, M and Γ are shown at the upper right.

The electronic states near the K and K′ points can be described by an effective-mass or $\boldsymbol{k} \cdot \boldsymbol{p}$ equation. In the following, we choose an $\boldsymbol{x}$–$\boldsymbol{y}$ coordinate system obtained by rotating the $\boldsymbol{x}'$–$\boldsymbol{y}'$ system by η, as shown in figure 1. Here, $\boldsymbol{x}$ and $\boldsymbol{y}$ represent the circumferential and axial directions of a SWNT, respectively, which are discussed later. The $\boldsymbol{k} \cdot \boldsymbol{p}$ equations around the K and K′ points of graphene are given by

$$\gamma\,(\hat{\boldsymbol{k}} \cdot \boldsymbol{\sigma})\boldsymbol{F}^{\mathrm{K}}(\boldsymbol{r}) = \varepsilon \boldsymbol{F}^{\mathrm{K}}(\boldsymbol{r}), \tag{1a}$$

$$\gamma\,(\hat{\boldsymbol{k}}' \cdot \boldsymbol{\sigma})\boldsymbol{F}^{\mathrm{K}'}(\boldsymbol{r}) = \varepsilon \boldsymbol{F}^{\mathrm{K}'}(\boldsymbol{r}), \tag{1b}$$

where γ is a band parameter, $\boldsymbol{\sigma} = (\sigma_x, \sigma_y)$ are the Pauli spin matrices, $\hat{\boldsymbol{k}} \equiv -\mathrm{i}\nabla$ is the wavevector operator ($\hat{k}'_x = \hat{k}_x$ and $\hat{k}'_y = -\hat{k}_y$) and ε is the energy. $\boldsymbol{F}^{\mathrm{K}}(\boldsymbol{r}) = [F^{\mathrm{K}}_{\mathrm{A}}(\boldsymbol{r}), F^{\mathrm{K}}_{\mathrm{B}}(\boldsymbol{r})]$ is an envelope function with two components representing the amplitudes at the A and B sites. The $\boldsymbol{k} \cdot \boldsymbol{p}$ equations can be derived from the tight-binding model [54] and the band parameter γ relates to the transfer integral γ_0 between nearest-neighbor carbon atoms as $\gamma = \sqrt{3}a\gamma_0/2$; they have the same form as the massless Dirac equation or Weyl equation for neutrinos. The energy bands around the K and K′ points of graphene are obtained from the $\boldsymbol{k} \cdot \boldsymbol{p}$ equations as

$$\varepsilon_s(\boldsymbol{k}) = s\gamma|\boldsymbol{k}|, \tag{2}$$

where $s = +1$ for the conduction band and -1 for the valence band. The energy bands of the graphene near the K and K′ points are degenerate and exhibit conic dispersion resembling the dispersion of light. Therefore, the band structure of graphene is called a Dirac cone.

2.1.2. Nanotubes. Any SWNT structure is determined by the chiral vector $\boldsymbol{L} = n_a\boldsymbol{a} + n_b\boldsymbol{b}$. The SWNT specified by $\boldsymbol{L}$ has a structure of rolled-up graphene such that two hexagons at the origin and at $\boldsymbol{L}$ overlap. Thus, the circumferential and axial directions agree with the $\boldsymbol{x}$ and $\boldsymbol{y}$ directions, respectively (see figure 1). Another choice of primitive translation vectors $\boldsymbol{a}_1 = \boldsymbol{a}$ and $\boldsymbol{a}_2 = \boldsymbol{a}+\boldsymbol{b}$ is also used to express the chiral vector, for example, $\boldsymbol{L} = n_1\boldsymbol{a}_1 + n_2\boldsymbol{a}_2$. An SWNT having vector $\boldsymbol{L}$ is usually called an (n_1, n_2) or (n_a, n_b) nanotube depending on the set of primitive translation vectors. The circumference length is given by

$$L = |\boldsymbol{L}| = a\sqrt{n_a^2 + n_b^2 - n_a n_b} = a\sqrt{n_1^2 + n_2^2 + n_1 n_2}, \quad (3)$$

and the chiral angle between the $\boldsymbol{x}$ and $\boldsymbol{x}'$ directions is given by

$$\eta = \cos^{-1}[(n_a - n_b/2)/L] = \cos^{-1}[(n_1 + n_2/2)/L]. \quad (4)$$

In the lowest-order approximation, the electronic states of a SWNT are obtained from the $\boldsymbol{k}\cdot\boldsymbol{p}$ equation (1) by imposing a periodic boundary condition along the circumferential direction. Because the wavefunction around the K point is given by $\psi^{\mathrm{K}}(\boldsymbol{r}) \propto \mathrm{e}^{\mathrm{i}\boldsymbol{K}\cdot\boldsymbol{r}}\boldsymbol{F}^{\mathrm{K}}(\boldsymbol{r})$, the periodic boundary condition $\psi^{\mathrm{K}}(\boldsymbol{r}+\boldsymbol{L}) = \psi^{K}(\boldsymbol{r})$ yields

$$\boldsymbol{F}^{\mathrm{K}}(\boldsymbol{r}+\boldsymbol{L}) = \boldsymbol{F}^{\mathrm{K}}(\boldsymbol{r}) \exp\left(-\mathrm{i}\frac{2\pi}{3}\nu\right), \quad (5)$$

where ν is an integer $(0, \pm 1)$ determined by

$$n_a + n_b = 3N + \nu, \quad (6)$$

with N being an integer. For the $\boldsymbol{a}_1, \boldsymbol{a}_2$ translational vectors, ν is determined by

$$n_1 - n_2 = 3N + \nu. \quad (7)$$

Similarly, the boundary condition for $\boldsymbol{F}^{\mathrm{K}'}(\boldsymbol{r})$ is given by

$$\boldsymbol{F}^{\mathrm{K}'}(\boldsymbol{r}+\boldsymbol{L}) = \boldsymbol{F}^{\mathrm{K}'}(\boldsymbol{r}) \exp\left(+\mathrm{i}\frac{2\pi}{3}\nu\right). \quad (8)$$

The envelope function is characterized by a plane wave $\boldsymbol{F}^{\mathrm{K}}(\boldsymbol{r}) \propto \exp(\mathrm{i}\boldsymbol{k}\cdot\boldsymbol{r})$. From the boundary condition (5), the discrete wavevector $k_x = \kappa_\nu(n)$ in the circumferential direction is obtained as

$$\kappa_\nu(n) = \frac{2\pi}{L}\left(n - \frac{\nu}{3}\right), \quad (9)$$

where n is an integer. We denote the continuous axial wavevector as $k = k_y$. The energy dispersion of a SWNT is obtained from that of a graphene by substituting $\boldsymbol{k} = [\kappa_\nu(n), k]$ into equation (2) [10]:

$$\varepsilon^{\mathrm{K}}_{s,n,k} = s\varepsilon(n, k), \quad (10)$$

where

$$\varepsilon(n, k) = \gamma\sqrt{\kappa_\nu(n)^2 + k^2}. \quad (11)$$

The corresponding envelope functions are written as

$$\boldsymbol{F}^{\mathrm{K}}_{s,n,k}(\boldsymbol{r}) = \frac{1}{\sqrt{AL}}\boldsymbol{F}^{\mathrm{K}}_{s,n,k}\exp[\mathrm{i}\kappa_\nu(n)x + \mathrm{i}ky], \quad (12)$$

where

$$\boldsymbol{F}^{\mathrm{K}}_{s,n,k} = \frac{1}{\sqrt{2}}\begin{bmatrix} b_\nu(n, k) \\ s \end{bmatrix}, \quad (13)$$

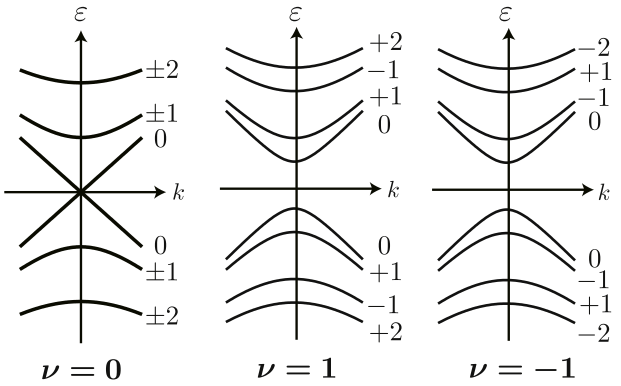

Figure 3. Energy bands of a SWNT near the Fermi energy. Numbers indicate band indices n. ν is specified by the chiral vector. For $\nu = 0$, band indices in the K and K′ valleys are the same and are labeled in the left panel. For $\nu = 1$ (-1), the band indices labeled in the middle and right panels indicate those in the K (K′) and K′ (K) valleys, respectively. A SWNT is metallic for $\nu = 0$ and semiconducting for $\nu = \pm 1$.

and

$$b_\nu(n, k) = \frac{\kappa_\nu(n) - \mathrm{i}k}{\sqrt{\kappa_\nu(n)^2 + k^2}}, \quad (14)$$

where A is the length of the SWNT.

Near the K′ point, the electronic states are obtained by replacing k with $-k$ (see equations (1*a*) and (1*b*) and the description below the equations) and ν by $-\nu$ (see equations (5) and (8)). Then, $\kappa'_\nu(n)$ and $b'_\nu(n, k)$ around the K′ point are given by $\kappa'_\nu(n) = \kappa_{-\nu}(n)$ and $b'_\nu(n, k) = b_{-\nu}(n, k)^*$, respectively.

The electronic states of a SWNT depend on the structure or chiral vector through the factor ν; a SWNT is metallic for $\nu = 0$ and semiconducting with a bandgap of $4\pi\gamma/3L$ for $\nu = \pm 1$. Figure 3 shows the band structures near the Fermi energy for $\nu = 0$, 1 and -1. The energy bands are specified by $s = \{\pm\}$ and n. In figure 3 each band is labeled with the band index n.

2.2. Aharonov–Bohm effect

In the presence of a magnetic flux ϕ passing through the cross section of a SWNT, a vector potential $\boldsymbol{A} = (\phi/L, 0)$ appears. This vector potential changes the boundary condition in the circumferential direction; consequently, $\kappa_\nu(n)$ is modified as follows:

$$\kappa_{\nu\varphi}(n) = \frac{2\pi}{L}\left(n + \varphi - \frac{\nu}{3}\right), \quad (15)$$

where $\varphi = \phi/\phi_0$ and $\phi_0 = ch/e$ is the magnetic flux quantum. Therefore, the energy levels of a SWNT are changed by $\kappa_{\nu\varphi}(n)$ [10]. In fact, the bandgaps at the K and K′ points are given by $\varepsilon^{\mathrm{K}}_{\mathrm{G}} = 2\gamma|\kappa_{\nu\varphi}(n)|$ and $\varepsilon^{\mathrm{K}'}_{\mathrm{G}} = 2\gamma|\kappa_{-\nu\varphi}(n)|$, respectively. The change in the bandgap is given by

$$\Delta\varepsilon_{\mathrm{G}}\ (\mathrm{meV}) = 0.49\ (\mathrm{T}^{-1}\ \mathrm{nm}^{-1})B\ (\mathrm{T})d\ (\mathrm{nm}), \quad (16)$$

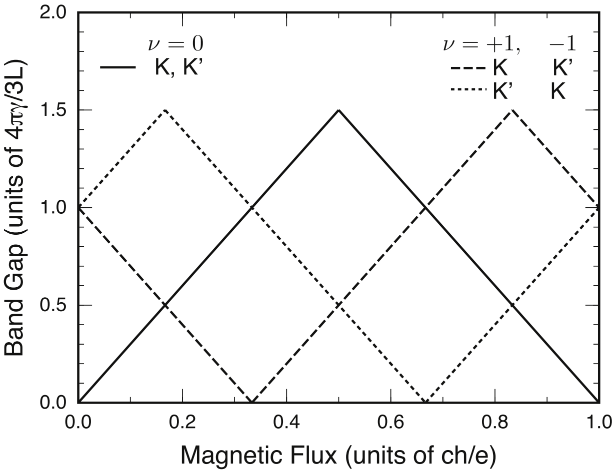

Figure 4. AB effect on bandgap of a SWNT. Bandgaps at the K and K′ points periodically change as a function of magnetic flux passing through the tube axis. The period of magnetic flux is the magnetic flux quantum $\phi_0 = ch/e$.

where B is a magnetic field, d is the SWNT diameter and $\gamma = 0.646$ eV nm is chosen. For $B = 10$ T, the bandgap change in a SWNT with $d = 1$ nm is 4.9 meV

Figure 4 shows the bandgap at the K and K′ points as a function of magnetic flux. The gap oscillates between 0 and $2\pi\gamma/L$ with a period of ϕ_0 because of the AB effect. For $\nu = 0$, the lowest-band edges at the K and K′ points are degenerate for any magnetic flux. For $\nu = \pm 1$, the band edges at the K and K′ points are degenerate at $\phi = 0$. However, the degeneracy is linearly and symmetrically lifted with increasing ϕ.

2.3. Higher-order correction

2.3.1. Trigonal warping. The $\boldsymbol{k}\cdot\boldsymbol{p}$ equation (1) describes the electronic states around the Fermi energy near the K and K′ points. In this region, the dispersion relation exhibits a conical structure; thus, each energy level is inversely proportional to the diameter. However, in the electronic states outside of this region, a constant-energy line changes from a circle to a warped closed curve with threefold symmetry. In the $\boldsymbol{k}\cdot\boldsymbol{p}$ scheme, the warping effect can be included by introducing a higher-order $\boldsymbol{k}\cdot\boldsymbol{p}$ term. The higher-order term H' of the $\boldsymbol{k}\cdot\boldsymbol{p}$ Hamiltonian in the K valley [59] is given by

$$H' = \gamma \frac{a}{4\sqrt{3}} \begin{pmatrix} 0 & \mathrm{e}^{3\mathrm{i}\eta}(\hat{k}_x + \mathrm{i}\hat{k}_y)^2 \\ \mathrm{e}^{-3\mathrm{i}\eta}(\hat{k}_x - \mathrm{i}\hat{k}_y)^2 & 0 \end{pmatrix}, \tag{17}$$

where η is the chiral angle depicted in figure 1. The Hamiltonian in the K′ valley is obtained by taking the complex conjugate and changing η to $\eta + \pi/3$ in equation (17). The resulting energy is degenerate in the K and K′ valleys, and the bandgap is calculated as [60]

$$\varepsilon_{\mathrm{G}}^{\mathrm{K}} \approx 2\gamma|\kappa_{\nu\varphi}(n)|\left[1 + \frac{a\kappa_{\nu\varphi}(n)}{4\sqrt{3}}\cos 3\eta\right]. \tag{18}$$

The warping effect does not modify the bandgap for armchair SWNTs ($\eta = \pi/6$), whereas the effect shifts the bandgap for zigzag SWNTs ($\eta = 0$) by the maximum amount.

2.3.2. Curvature effect. Curvature in the circumferential direction causes the origin of $\hat{\boldsymbol{k}}$ to shift in the $\boldsymbol{k}\cdot\boldsymbol{p}$ Hamiltonian [61, 62]. This shift in the circumferential or $\boldsymbol{x}$ direction can be represented by an effective magnetic flux ϕ_{eff} passing through the cross section, i.e. $\Delta k_x = (2\pi/L)(\phi_{\mathrm{eff}}/\phi_0)$. The effective flux has different signatures in the K and K′ valleys. For the K valley, the effective flux is estimated as [62]

$$\varphi \equiv \frac{\phi_{\mathrm{eff}}}{\phi_0} = -\frac{2\pi}{4\sqrt{3}}\frac{a}{L}p\cos 3\eta, \tag{19}$$

where $p = 1 - (3/8)(\gamma'/\gamma)$, $\gamma' = -(\sqrt{3}/2)V_{\mathrm{pp}}^{\pi}a$ and $\gamma = -(\sqrt{3}/2)(V_{\mathrm{pp}}^{\sigma} - V_{\mathrm{pp}}^{\pi})a$; V_{pp}^{π} and V_{pp}^{σ} are the conventional tight-binding parameters for neighboring p orbitals. The curvature effect becomes largest in zigzag SWNTs ($\eta = 0$). For typical parameters, we have $\gamma'/\gamma \sim 8/3$; therefore, it is very difficult to estimate p reliably except that $|p| < 1$. The curvature effect opens a small gap for metallic SWNT except for armchair SWNTs ($\eta = \pi/6$). The gap becomes largest for zigzag SWNTs ($\eta = 0$).

The curvature and trigonal warping effects both depend on the chiral angle η; this is why the electronic states of a SWNT depend on the chirality. Like the curvature effect, the warping effect also becomes larger for thin SWNTs because of the large level separation due to size quantization. Although some SWNTs with different chiralities have fairly similar diameters, the warping and curvature effects magnify the level difference for these SWNTs. Therefore, a so-called family pattern appears when the optical transition energies are summarized as a function of the diameter for various chiral vectors [63–66]. This fact makes it easy to assign a chiral vector to an individual SWNT from resonant optical spectra such as PL and resonant Raman spectra.

2.3.3. Effective overlap integral. The overlap integral between nearest-neighbor atomic wavefunctions yields an asymmetric band structure between the conduction and valence bands of a graphene [67]. The effective-mass equation including the overlap integral is given by

$$\begin{pmatrix} -\varepsilon & (\gamma + \varepsilon S)\hat{f}(\hat{k}) \\ (\gamma + \varepsilon S)\hat{f}(\hat{k})^* & -\varepsilon \end{pmatrix} \begin{pmatrix} F_{\mathrm{A}}^{\mathrm{K}} \\ F_{\mathrm{B}}^{\mathrm{K}} \end{pmatrix} = 0, \tag{20}$$

where $S = (\sqrt{3}a/2)S_0$ and S_0 is the overlap integral. The operator $\hat{f}(\hat{k})$ is defined as

$$\hat{f}(\hat{k}) = (\hat{k}_x - \mathrm{i}\hat{k}_y) + \frac{a}{4\sqrt{3}}\mathrm{e}^{3\mathrm{i}\eta}(\hat{k}_x + \mathrm{i}\hat{k}_y)^2, \tag{21}$$

where the first and second terms represent the operators for the lowest- and higher-order $\boldsymbol{k}\cdot\boldsymbol{p}$ approximations, respectively [66]. The overlap integral of a graphene is $S_0 \approx 0.13$.

The energy of a graphene in the K valley is obtained as

$$\varepsilon_s^{\mathrm{K}} = s\frac{\gamma|f(k)|}{1 - sS|f(k)|}. \tag{22}$$

The energy bandwidth of the conduction band is larger than that of the valence band of graphene. Thus, the overlap

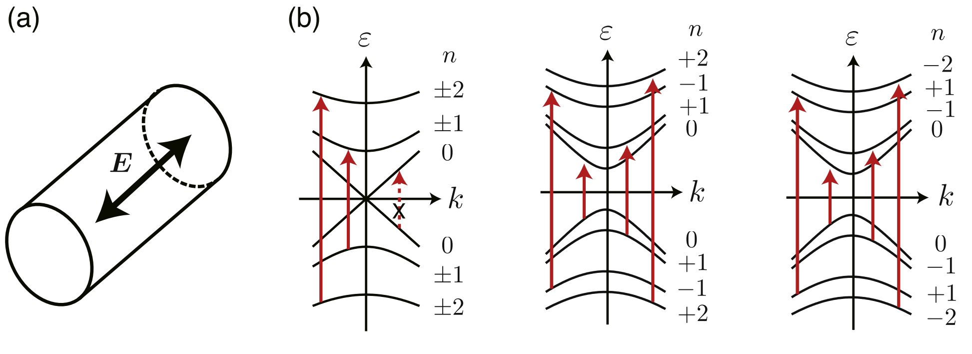

metal（K,K'） semiconductor（K） semiconductor（K'）

Figure 5. (a) Schematic illustration of light polarized parallel to the tube axis. (b) Energy bands and allowed optical transitions (red arrows) for metallic and semiconducting SWNTs. Band indices of semiconducting SWNT in middle and right panels are labeled for $\nu = +1$. Band indices for $\nu = -1$ are obtained by reversing the signs.

integral produces an asymmetry between the conduction and valence bands. The wavefunctions are given by

$$\boldsymbol{F}_s^{\mathrm{K}} = \frac{1}{\sqrt{2}} \begin{pmatrix} f(k)/|f(k)| \\ s \end{pmatrix}. \tag{23}$$

The wavefunction is independent of the overlap integral.

The energy and wavefunctions of a SWNT are obtained by substituting $\boldsymbol{k} = [\kappa_\nu(n), k]$ into equations (22) and (23), respectively. Because of the asymmetry between the conduction and valence bands, the level separation of the conduction bands of a SWNT is larger than that of the valence bands. The difference in the level separation causes a quasi-dark exciton for light polarization perpendicular to the tube axis (see section 6.4). A next-nearest-neighbor hopping integral in a tight-binding model also contributes to the band asymmetry. This parameter can be included in the $\boldsymbol{k} \cdot \boldsymbol{p}$ equation in the same form as the overlap integral [66]. Therefore, the next-nearest hopping integral and the overlap integral are summarized by a single parameter S as the effective overlap integral.

3. Optical selection rules

The optical selection rules of a SWNT depend on the direction of light polarization because of its cylindrical structure. In this section, the optical selection rules for light polarization parallel and perpendicular to the tube axis are discussed.

3.1. Dynamical conductivity

The optical absorption is related to the dynamical conductivity, which is calculated from linear response theory. It is useful to expand the electric field $E_\xi(\theta, \omega)$ and induced current density $j_\xi(\theta, \omega)$ into a Fourier series:

$$E_\xi(\theta, \omega) = \sum_l E_\xi^l(\omega) \exp(\mathrm{i}l\theta - \mathrm{i}\omega t), \tag{24}$$

$$j_\xi(\theta, \omega) = \sum_l j_\xi^l(\omega) \exp(\mathrm{i}l\theta - \mathrm{i}\omega t), \tag{25}$$

where ξ denotes x or y, and the azimuth $\theta = 2\pi x/L$ represents the position in the circumferential direction. In the linear response regime, the induced current density is written as

$$j_\xi^l(\omega) = \sigma_{\xi\xi}^l(\omega) E_\xi^l(\omega), \tag{26}$$

where $\sigma_{\xi\xi}^l(\omega)$ is the dynamical conductivity.

The dynamical conductivity at zero temperature in a rotating-wave approximation is calculated using the Kubo formula as

$$\sigma_{\xi\xi}^l(\omega) = \frac{2\hbar}{\mathrm{i}AL} \sum_{\mathrm{KK}'} \sum_{n,k} \sum_{s,s'} \frac{1}{\varepsilon_{s,n,k} - \varepsilon_{s',n+l,k}} \times \frac{|\langle s, n, k|\hat{j}_\xi^l|s', n+l, k\rangle|^2}{\varepsilon_{s,n,k} - \varepsilon_{s',n+l,k} - \hbar\omega - \mathrm{i}\Gamma}, \tag{27}$$

where $|s, n, k\rangle$ represents the envelope function $\boldsymbol{F}_{s,n,k}^{\mathrm{K}}$ or $\boldsymbol{F}_{s,n,k}^{\mathrm{K}'}$, Γ is a phenomenological damping energy and the factor 2 comes from the spin degeneracy.

The current operator $\hat{j}_\xi^l$ in the K valley is given by

$$\hat{j}_\xi^l = -\frac{e}{\mathrm{i}\hbar}[\hat{\xi}, \gamma\boldsymbol{\sigma} \cdot \hat{\boldsymbol{k}}]\mathrm{e}^{-\mathrm{i}l\theta} = -\frac{e\gamma}{\hbar}\sigma_\xi \mathrm{e}^{-\mathrm{i}l\theta}, \tag{28}$$

where $\hat{\xi} = \hat{x}$ or $\hat{y}$. In the K′ valley, the operator $\hat{j}_x^l$ is the same as that in the K valley, but j_y^l has the opposite sign of that in the K valley. The factor $|\langle s, n, k|\hat{j}_\xi^l|s', n+l, k\rangle|^2$ provides the same value for both the K and K′ valleys.

3.2. Parallel polarization

When the polarization of an external electric field $\boldsymbol{D}$ is parallel to the tube axis as shown in figure 5(a), the electric field on the cylindrical surface is constant; i.e. the Fourier component of the electric field is written as

$$D_y^l = D\delta_{l,0}. \tag{29}$$

The relevant induced current is $j_y^{l=0}(\omega)$; thus, the optical transition becomes allowed between bands with the same band index.

One exception to the above statement exists; the optical transition is forbidden for metallic SWNTs between the linear

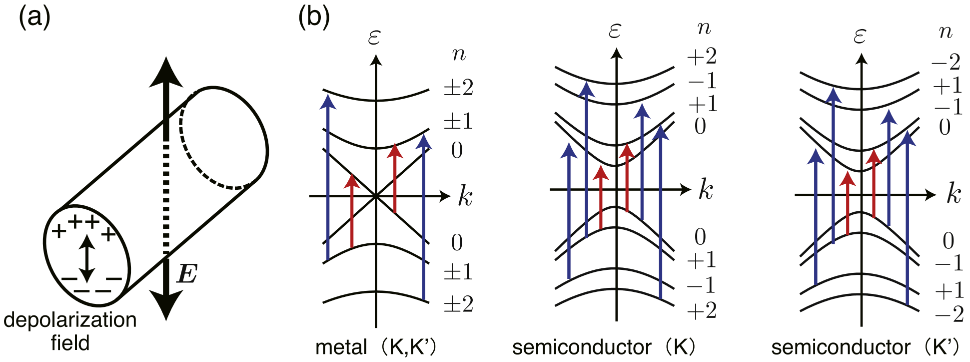

Figure 6. (a) Schematic illustration of light polarized perpendicular to the tube axis. Depolarization charge and field are depicted. (b) Energy bands and allowed optical transitions are indicated by arrows for metallic and semiconducting SWNTs. Red and blue arrows indicate allowed and forbidden transitions at the band edge, respectively. Band indices of semiconducting SWNT in the middle and right panels are labeled for $\nu = +1$. Band indices for $\nu = -1$ are obtained by reversing the signs.

conduction and valence bands. To demonstrate this fact, we calculate the matrix elements of the current operator:

$$\langle +, n, k|\hat{j}_y^{l=0}|-, n, k\rangle = \frac{1}{2}\frac{e\gamma}{\hbar}[b_\nu(n,k)^* + b_\nu(n,k)]. \quad (30)$$

Because $b_\nu(n,k) = -\mathrm{i}$ for the band index $n = 0$ of metallic SWNT, $|\langle +, 0, k|\hat{j}_y^{l=0}|-, 0, k\rangle|^2 = 0$; i.e. the optical transition is forbidden. A more sophisticated understanding is as follows: the wavefunction is an eigenfunction of σ_y (see equations (1*a*) and (1*b*)) for the band index $n = 0$ of a metallic SWNT. The electronic states of the conduction and valence bands of a metallic SWNT having $n = 0$ are orthogonalized with each other; therefore, the matrix element $j_y \propto \sigma_y$ between them becomes zero.

Figure 5(b) shows the allowed optical transitions (red arrows) of metallic and semiconducting SWNTs for parallel polarization.

3.3. Perpendicular polarization

The optical selection rules for perpendicular polarization differ from those for parallel polarization. When the polarization of the external field is perpendicular to the tube axis as shown in figure 6(a), the electric field on the cylindrical surface changes sinusoidally as $\boldsymbol{D} = (D\sin\theta, 0)$, i.e. the Fourier component of the electric field is written as

$$D_x^l = \frac{D}{2\mathrm{i}}\delta_{l,1} - \frac{D}{2\mathrm{i}}\delta_{l,-1}. \quad (31)$$

The relevant induced current density is $j_x^{l=\pm1}(\omega)$, so optical transitions are allowed between bands having band indices that differ by ±1. At the band edges, however, transitions having a finite current matrix element are limited. For $k = 0$, the matrix elements of the current operator are calculated as

$$\langle +, n, 0|\hat{j}_x^{l=\pm1}|-, n\pm1, 0\rangle$$
$$= \frac{1}{2}\frac{e\gamma}{\hbar}\{-\mathrm{sgn}[\kappa_\nu(n)] + \mathrm{sgn}[\kappa_\nu(n\pm1)]\}, \quad (32)$$

where $\mathrm{sgn}(\kappa)$ denotes the sign of κ. Then, the matrix elements become finite for opposite signs between $\kappa_\nu(n)$ and $\kappa_\nu(n\pm1)$ and zero for identical signs. Other transitions at the band edges are all forbidden. Because the density of states at the band edges of a quasi-1D system exhibit divergence as $\sqrt{\varepsilon - \varepsilon(n, k=0)}$ in the limit of $\Gamma = 0$, absorptions corresponding to the band-edge forbidden transitions are quite small as shown in figure 14 (the large and small peaks correspond to band-edge allowed and forbidden transitions, respectively). A more sophisticated understanding is as follows: the wavefunctions at the band edge ($k = 0$) are eigenfunctions of σ_x (see equations (1*a*) and (1*b*)) and $j_x \propto \sigma_x$. Thus, optical transitions between band-edge states having the same eigenvalue of σ_x are allowed, and those with different eigenvalues are forbidden. Equation (13) reveals that two envelope functions belong to the same eigenvalue of σ_x when the $\kappa_\nu(n)$ values in the conduction and valence bands have opposite signs.

Figure 6(b) shows the allowed optical transitions of metallic and semiconducting SWNTs for perpendicular polarization. Red and blue arrows indicate allowed and forbidden transitions at the band edge, respectively.

4. Excitons

Exciton effects are generally important in low-dimensional systems such as a SWNT. The exciton states of a SWNT were first discussed theoretically by Ando [68], who used the screened Hartree–Fock approximation in the $\boldsymbol{k}\cdot\boldsymbol{p}$ scheme. First-principles studies of exciton states have also been performed [69–71]. The resulting binding energy reaches a few hundred millielectronvolts. Because of this large binding energy, the excitons in a SWNT can be observed at room temperature. The exciton effect in SWNTs was first indicated experimentally by absorption spectra of a thin film containing SWNTs [33, 72], in which the existence of excitons was deduced from the difference between the observed absorption peaks and the energies calculated in a simple tight-binding model. Similarly, the ratio problem was pointed out as evidence of the effect of excitons on optical spectra [73]. The ratio of E_{22}^S/E_{11}^S becomes 2 in the large-diameter limit within the tight-binding model, where E_{nn}^S denotes the excitation energy from the nth highest valence to the nth lowest conduction bands of a semiconducting SWNT. However, the ratio approaches ~1.7 in the extrapolation from the PLE mapping data [11, 63]. The ratio problem can be resolved by considering the exciton effect.

More reliable evidence of excitons has been demonstrated by two-photon PLE [74, 75]. The typical absorption and PL spectra are observed as a one-photon process. However, at high excitation power densities, two-photon absorption occurs. The selection rules for two-photon absorption differ from those of one-photon absorption; thus, complementary information of excitons is obtained from the two-photon absorption. In a quasi-1D material such as SWNTs, a Rydberg series of exciton states below the bandgap is classified by symmetry with respect to reflection through a plane perpendicular to the tube axis [76]. The even-parity (odd-parity) states are denoted by 1s, 2s, etc (2p, 3p, etc), and they are allowed for one-photon (two-photon) absorption. In the PLE map for two-photon excitation, the bound-state nature of excitons was demonstrated by the observation of distinct fluorescence emission from the 2p exciton. When the experimental results and theoretical calculations are combined, the exciton binding energies are found to be 0.3–0.4 eV for SWNTs having diameters between 6.8 and 9.0 Å [74, 75]. A detailed theoretical study of two-photon absorption has been performed [77].

This section gives a brief review of the exciton states of a SWNT. The calculation method developed by Ando [68] is described in sections 4.1 and 4.2. In section 4.3, a dynamical e–h EXI is introduced [78]. This dynamical character of the e–h EXI is important for calculating the exciton wavefunction and absorption spectra, as shown in section 6.2. The fine structure originating from short-range interaction is summarized in section 4.4. The exciton states for parallel and perpendicular polarization are described in sections 4.5 and 4.6, respectively.

4.1. Hartree–Fock approximation

The Hamiltonian of interacting electrons in the second quantized form is written as

$$H = \int \mathrm{d}\boldsymbol{r}\, \hat{\Psi}^\dagger(\boldsymbol{r}) h(\boldsymbol{r}) \hat{\Psi}(\boldsymbol{r}) + \frac{1}{2}\int \mathrm{d}\boldsymbol{r} \int \mathrm{d}\boldsymbol{r}'\, \hat{\Psi}^\dagger(\boldsymbol{r})\hat{\Psi}^\dagger(\boldsymbol{r}') v(\boldsymbol{r}-\boldsymbol{r}')\hat{\Psi}(\boldsymbol{r}')\hat{\Psi}(\boldsymbol{r}), \tag{33}$$

where $h(\boldsymbol{r})$ is the kinetic term, $v(\boldsymbol{r}-\boldsymbol{r}')$ is the Coulomb interaction between electrons and $\Psi^\dagger(\boldsymbol{r})$ [$\Psi(\boldsymbol{r})$] is a creation (annihilation) field operator. The field operator for a SWNT is expanded as

$$\hat{\Psi}(\boldsymbol{r}) = \sum_{\zeta=K,K'} \sum_{\alpha=(\pm,n)} \sum_k \boldsymbol{F}^\zeta_{\alpha k}(\boldsymbol{r}) c^\zeta_{\alpha k}, \tag{34}$$

where $\boldsymbol{F}^\zeta_{\alpha k}(\boldsymbol{r})$ is defined in equation (12) with $\alpha = (s, n)$ and $c^\zeta_{\alpha k}$ is an annihilation operator.

In the Hartree–Fock approximation, the ground state $|g\rangle$ of a SWNT is given by

$$|g\rangle = \prod_{\zeta n k} c^{\zeta\dagger}_{-,n,k}|0\rangle, \tag{35}$$

where $|0\rangle$ is a vacuum state and $c^{\zeta\dagger}_{-,n,k}$ is the creation operator for a valence electron.

A one-electron excitation state is generated by absorbing one photon, which excites a valence electron $|-, n, k\rangle$ to a conduction state $|+, n+l, k'\rangle$. Because the wavevector of the photon is much smaller than $\boldsymbol{K} - \boldsymbol{K}'$, excitation between different valleys (K and K′) can be neglected. In addition, we approximate $k' \approx k$. Then the one-electron excitation states $|\Lambda, l\rangle$ are written as

$$|\Lambda, l\rangle = B^\dagger_{\Lambda,l}|g\rangle, \tag{36}$$

where

$$B^\dagger_{\Lambda,l} = \sum_{\zeta n k} \psi^\zeta_{\Lambda,l}(n,k) c^{\zeta\dagger}_{+,n+l,k} c^\zeta_{-,n,k}|g\rangle. \tag{37}$$

The equation of motion for $|\Lambda, l\rangle$ is calculated from

$$\begin{aligned}(H - \bar{E}^l_\Lambda)|\Lambda, l\rangle &= (HB^\dagger_{\Lambda,l} - \bar{E}^l_\Lambda B^\dagger_{\Lambda,l})|g\rangle \\ &= ([H, B^\dagger_{\Lambda,l}] + \bar{E}_g B^\dagger_{\Lambda,l} - \bar{E}^l_\Lambda B^\dagger_{\Lambda,l})|g\rangle \\ &= 0,\end{aligned} \tag{38}$$

where $\bar{E}^l_\Lambda$ and $\bar{E}_g$ are the energies of $|\Lambda, l\rangle$ and $|g\rangle$, respectively. Therefore, we have

$$[H, B^\dagger_{\Lambda,l}]|g\rangle = E^l_\Lambda B^\dagger_{\Lambda,l}|g\rangle, \tag{39}$$

where $E^l_\Lambda = \bar{E}^l_\Lambda - \bar{E}_g$ is the excitation energy. By applying $\langle g|c^{\zeta\dagger}_{-,n,k} c^\zeta_{+,n+l,k}$ to equation (39) from the left-hand side, the equation for $\psi^\zeta_{\Lambda,l}(n,k)$ is obtained as

$$\sum_{n'k'} H^{\zeta\zeta'}_{(nk)(n'k')} \psi^{\zeta'}_{\Lambda,l}(n',k') = E^l_\Lambda \psi^\zeta_{\Lambda,l}(n,k), \tag{40}$$

where

$$\begin{aligned}H^{\zeta\zeta'}_{(nk)(n'k')} &= [E^\zeta_{+,n+l,k} - E^\zeta_{-,n,k}]\delta_{\zeta\zeta'}\delta_{nn'}\delta_{kk'} \\ &\quad - v^{\zeta\zeta\zeta\zeta}_{(+,n+l,k;+,n'+l,k')(-,n',k';-,n,k)}\delta_{\zeta\zeta'} \\ &\quad + v^{\zeta\zeta\zeta'\zeta'}_{(+,n+l,k;-,n,k)(-,n',k';+,n'+l,k')},\end{aligned} \tag{41}$$

with

$$\begin{aligned}v^{\zeta_1\zeta_2\zeta_3\zeta_4}_{(\alpha_1 k_1;\alpha_2 k_2)(\alpha_3 k_3;\alpha_4 k_4)} &= \int \mathrm{d}\boldsymbol{r} \int \mathrm{d}\boldsymbol{r}'\, \boldsymbol{F}^{\zeta_1 *}_{\alpha_1,k_1}(\boldsymbol{r}) \boldsymbol{F}^{\zeta_2}_{\alpha_2,k_2}(\boldsymbol{r}) \\ &\quad \times v(\boldsymbol{r}-\boldsymbol{r}') \boldsymbol{F}^{\zeta_3 *}_{\alpha_3,k_3}(\boldsymbol{r}') \boldsymbol{F}^{\zeta_4}_{\alpha_4,k_4}(\boldsymbol{r}').\end{aligned} \tag{42}$$

In the first term of equation (41), $E^\zeta_{s,n,k}$ represents a single-particle energy in the $\zeta = \{\mathrm{K}, \mathrm{K}'\}$ valley, including the self-energy:

$$\begin{aligned}E^\zeta_{\pm,n,k} &= \pm\gamma\sqrt{\kappa_\nu(n)^2 + k^2} \\ &\quad - \sum_{n',k'} v^{\zeta\zeta\zeta\zeta}_{(\pm,n,k;-,n',k')(-,n',k';\pm,n,k)},\end{aligned} \tag{43}$$

where the last term represents the self-energy coming from an exchange Coulomb interaction. A direct Coulomb interaction, which has only a Fourier component with $\boldsymbol{q} = 0$, is cancelled by Coulomb interaction with the positive background. The second and last terms in equation (41) represent electron–hole (e–h) direct Coulomb interaction and e–h EXI, respectively. In the $\boldsymbol{k}\cdot\boldsymbol{p}$ scheme, only the long-range part of the interactions is considered, so there is no e–h direct Coulomb interaction between states in the K and K′ valleys. However, a finite e–h EXI occurs between states in the K and K′ valleys. Note that both the direct e–h Coulomb interaction and the e–h EXI between states in the K and K′ valleys also appear as a short-range part. These short-range parts provide fine structure of exciton levels discussed in section 4.4.

The Coulomb potential between two electrons on the cylindrical surface at $\boldsymbol{r}$ and $\boldsymbol{r}'$ is written as

$$v(\boldsymbol{r}-\boldsymbol{r}') = \sum_q \exp\left[\mathrm{i}q(y-y')\right] \times \frac{2e^2}{\kappa A} K_0\left(\frac{L|q|}{2\pi}\left|2\sin\frac{\pi(x-x')}{L}\right|\right), \tag{44}$$

where $K_n(t)$ is a modified Bessel function of the second kind. Then the Coulomb matrix elements are given by

$$v^{\zeta\zeta\zeta'\zeta'}_{(\alpha,k+q;\beta,k)(\beta',k';\alpha',k'+q)} = v_{n-m}(q)\delta_{n-m,n'-m'}(\boldsymbol{F}^{\zeta *}_{\alpha,k+q}\cdot\boldsymbol{F}^{\zeta}_{\beta,k}) \times(\boldsymbol{F}^{\zeta' *}_{\beta',k'}\cdot\boldsymbol{F}^{\zeta'}_{\alpha',k'+q}), \tag{45}$$

with

$$v_{n-m}(q) = \frac{2e^2}{\kappa} I_{|n-m|}\left(\frac{L|q|}{2\pi}\right) K_{|n-m|}\left(\frac{L|q|}{2\pi}\right), \tag{46}$$

where $I_n(t)$ is the modified Bessel function of the first kind and $\alpha = (s, n)$, $\beta = (s', m)$.

4.2. Screened-Hartree–Fock approximation

In the conventional random-phase approximation or self-consistent field approximation, the screening effect of electrons appears in the direct Coulomb interaction. The screened direct Coulomb potential is given by

$$V^{\zeta\zeta\zeta\zeta}_{(\alpha,k+q;\beta,k)(\beta',k';\alpha',k'+q)} = \frac{v^{\zeta\zeta\zeta\zeta}_{(\alpha,k+q;\beta,k)(\beta',k';\alpha',k'+q)}}{\varepsilon_{n-m}(q)}, \tag{47}$$

where $\varepsilon_{n-m}(q)$ is the dielectric function:

$$\varepsilon_{n-m}(q) = 1 + v_{n-m}(q)\Pi_{n-m}(q), \tag{48}$$

with $\Pi_{n-m}(q)$ being the polarization function:

$$\Pi_{n-m}(q) = -\frac{2}{A}\sum_{\zeta=\mathrm{K},\mathrm{K}'}\sum_{n'm'}\sum_{k'}\delta_{n-m,n'-m'} \times|\boldsymbol{F}^{\zeta *}_{\alpha,k}\cdot\boldsymbol{F}^{\zeta}_{\beta,k+q}|^2 \frac{g_0(\varepsilon^{\zeta}_{+,m',k'})g_0(\varepsilon^{\zeta}_{-,n',-k'+q})}{\varepsilon^{\zeta}_{-,n',-k'+q}-\varepsilon^{\zeta}_{+,m',k'}}. \tag{49}$$

We have introduced a cutoff function $g_0(\varepsilon)$:

$$g_0(\varepsilon) = \frac{\varepsilon}{|\varepsilon|^{\alpha_{\mathrm{c}}}+\varepsilon_{\mathrm{c}}^{\alpha_{\mathrm{c}}}}, \tag{50}$$

which contains two parameters α_{c} and ε_{c} and should be chosen in such a way that only the contributions from states near the Fermi energy, where the $\boldsymbol{k}\cdot\boldsymbol{p}$ scheme is valid, are considered.

In the screened Hartree–Fock approximation, the direct Coulomb potential $v^{\zeta\zeta\zeta\zeta}_{(\alpha,k+q;\beta,k)(\beta',k';\alpha',k'+q)}$ is replaced by the screened one $V^{\zeta\zeta\zeta\zeta}_{(\alpha,k+q;\beta,k)(\beta',k';\alpha',k'+q)}$ in the matrix elements (41) in the Hartree–Fock approximation. Note that the e–h EXI is not screened by $\varepsilon_{n-m}(q)$ [79]. Then, the matrix elements in the screened Hartree–Fock approximation are written as

$$\begin{aligned} H^{\zeta\zeta'}_{(nk)(n'k')} &= [E^{\zeta}_{+,n+l,k} - E^{\zeta}_{-,n,k}]\delta_{\zeta\zeta'}\delta_{nn'}\delta_{kk'} \\ &\quad - V^{\zeta\zeta\zeta\zeta}_{(+,n+l,k;+,n'+l,k')(-,n',k';-,n,k)}\delta_{\zeta\zeta'} \\ &\quad + v^{\zeta\zeta\zeta'\zeta'}_{(+,n+l,k;-,n,k)(-,n',k';+,n'+l,k')}. \end{aligned} \tag{51}$$

4.3. Dynamical electron–hole exchange interaction

The e–h EXI can be interpreted as an interaction between the exciton and the depolarization field caused by the exciton [80–83]. In a linear response regime, the depolarization field should oscillate with the applied field frequency. Consequently, the frequency should appear in the e–h EXI for the optically excited exciton. However, such a factor is not included in the conventional e–h EXI in the last term of equation (51). In fact, the optical absorption of an exciton calculated from the conventional e–h EXI is quite different from that calculated including the depolarization effect (see the red solid and dashed lines in figure 14(b)).

A general form of a correct e–h EXI for a SWNT is given by

$$A^{\mathrm{EXI}}_{uu',l}(\omega) = \frac{\mathrm{i}\hbar}{\varepsilon^{l}_{u'}}\int \mathrm{d}\boldsymbol{r}\int\mathrm{d}\boldsymbol{r}'\langle u,l|\hat{\boldsymbol{j}}(\boldsymbol{r})|g\rangle \cdot\bar{\boldsymbol{G}}^{L}(\boldsymbol{r},\boldsymbol{r}')\cdot\langle g|\hat{\boldsymbol{j}}(\boldsymbol{r}')|u',l\rangle, \tag{52}$$

where $|u,l\rangle$ and ε^{l}_{u} denote an exciton state and its energy, respectively, and they are obtained excluding the e–h EXI in the K or K′ valley, in which u includes valley information (K or K′ valley). $\bar{\boldsymbol{G}}^{L}(\boldsymbol{r},\boldsymbol{r}')$ is the longitudinal part of a dyadic Green function for the Maxwell equations. The derivation of this form will be provided briefly in section 5.1. The longitudinal component $\bar{\boldsymbol{G}}^{L}$ is generally given by $\bar{\boldsymbol{G}}^{L}(\boldsymbol{r},\boldsymbol{r}') = [\mathrm{i}/(\omega\kappa)]\nabla 1/|\boldsymbol{r}-\boldsymbol{r}'|\nabla'$, where κ is the background dielectric constant. Substituting the explicit form of $\bar{\boldsymbol{G}}^{L}$ into equation (52) and using the continuity equation $[\hat{\rho}, H]/\mathrm{i}\hbar + \nabla\cdot\hat{\boldsymbol{j}} = 0$, where $\hat{\rho}$ is a charge-density operator, we have

$$A^{\mathrm{EXI}}_{uu',l}(\omega) = \frac{1}{\kappa}\frac{\varepsilon^{l}_{u}}{\hbar\omega}\int\mathrm{d}\boldsymbol{r}\int\mathrm{d}\boldsymbol{r}'\,\frac{\langle u,l|\hat{\rho}(\boldsymbol{r})|g\rangle\langle g|\hat{\rho}(\boldsymbol{r}')|u',l\rangle}{|\boldsymbol{r}-\boldsymbol{r}'|}. \tag{53}$$

On the other hand, the conventional e–h EXI $A^{\mathrm{EXI(c)}}_{uu'}$ given in the last term of equation (51) has the following form:

$$A^{\mathrm{EXI(c)}}_{uu',l} = \frac{1}{\kappa}\int\mathrm{d}\boldsymbol{r}\int\mathrm{d}\boldsymbol{r}'\,\frac{\langle u,l|\hat{\rho}(\boldsymbol{r})|g\rangle\langle g|\hat{\rho}(\boldsymbol{r}')|u',l\rangle}{|\boldsymbol{r}-\boldsymbol{r}'|}. \tag{54}$$

Note that the e–h EXI equation (53) has an extra factor $\varepsilon^{l}_{u}/\hbar\omega$ compared to the conventional e–h EXI. Thus, we call it a dynamical e–h EXI.

4.4. Fine structure

A conduction electron and valence hole form an exciton owing to the long-range direct Coulomb term. Because electron and hole states have two valleys at the K and K′ points with twofold spin degeneracy, the exciton states have 16-fold degeneracy [84]. We denote $|(\mathrm{K},\uparrow)(\mathrm{K}',\downarrow)\rangle$ as an exciton consisting of a K-valley electron with spin up and a K′-valley hole with spin down. Here, the spin of a hole is denoted by that of the corresponding electron in the valence band. Therefore, the hole spin notation is opposite to that frequently used.

The 16 states are classified into singlets and triplets with respect to the total spin. The four singlet states are as follows:

$$^1|\zeta\zeta'\rangle = \frac{1}{\sqrt{2}}[|(\zeta,\uparrow)(\zeta',\uparrow)\rangle + |(\zeta,\downarrow)(\zeta',\downarrow)\rangle], \qquad (55)$$

where $\zeta, \zeta' = \mathrm{K}$ or K', respectively. The 12 triplet states are as follows:

$$\begin{aligned} ^3|\zeta\zeta', +1\rangle &= |(\zeta,\uparrow)(\zeta',\downarrow)\rangle, \\ ^3|\zeta\zeta', 0\rangle &= \frac{1}{\sqrt{2}}[|(\zeta,\uparrow)(\zeta',\uparrow)\rangle - |(\zeta,\downarrow)(\zeta',\downarrow)\rangle], \qquad (56) \\ ^3|\zeta\zeta', -1\rangle &= |(\zeta,\downarrow)(\zeta',\uparrow)\rangle. \end{aligned}$$

The degeneracy of the singlet and triplet excitons is generally lifted by the e–h EXI; thus, the energy of the singlet exciton is higher than that of the triplet states. Further, some degeneracies are lifted by a weak short-range direct Coulomb interaction and the e–h EXI, which causes interaction between an electron and a hole in different valleys. As a result, the singlet excitons split into bonding and anti-bonding states:

$$^1|\mathrm{KK}-\mathrm{K}'\mathrm{K}'(\pm)\rangle = \frac{1}{\sqrt{2}}(^1|\mathrm{KK}\rangle \pm {}^1|\mathrm{K}'\mathrm{K}'\rangle), \qquad (57)$$

and two degenerate states given by $^1|\mathrm{KK}'\rangle$ and $^1|\mathrm{K}'\mathrm{K}\rangle$ [84]. The degeneracy of the triplet excitons splits in the same way although each state has a threefold degeneracy corresponding to the degree of the magnetic quantum number for total spin 1. Among the 16 states, the only optically allowed level is $^1|\mathrm{KK}-\mathrm{K}'\mathrm{K}'(+)\rangle$ and the other states are all forbidden.

Precisely speaking, the anti-bonding states $^1|\mathrm{KK}-\mathrm{K}'\mathrm{K}'(-)\rangle$ between excitons in the K and K′ valleys are not true forbidden states for polarization perpendicular to the tube axis but have a small oscillator strength. In fact, weak PLE signals have been observed for perpendicular polarization [85]. This $^1|\mathrm{KK}-\mathrm{K}'\mathrm{K}'(-)\rangle$ exciton with perpendicular polarization is called a quasi-dark state. This feature arises from the asymmetry between the conduction and valence bands due to the effective overlap integral (see section 2.3.3). As a result, an energy difference between excitons in the K and K′ valleys exist for perpendicular polarization. For parallel polarization, however, there is no energy difference between excitons in the K and K′ valleys, so the exciton $^1|\mathrm{KK}-\mathrm{K}'\mathrm{K}'(-)\rangle$ with parallel polarization becomes a dark state. This is discussed in detail in section 6.4.

4.5. Parallel polarization

Exciton states generated by polarized light parallel to the tube axis are calculated from the screened Hartree–Fock approximation (51) [68]. Because of the Fourier component (29) of parallel polarization, exciton states with $l = 0$ in equation (37) are excited. Note that the e–h EXI $A^{\mathrm{EXI}}_{uu',l}(\omega)$ becomes zero for parallel polarization.

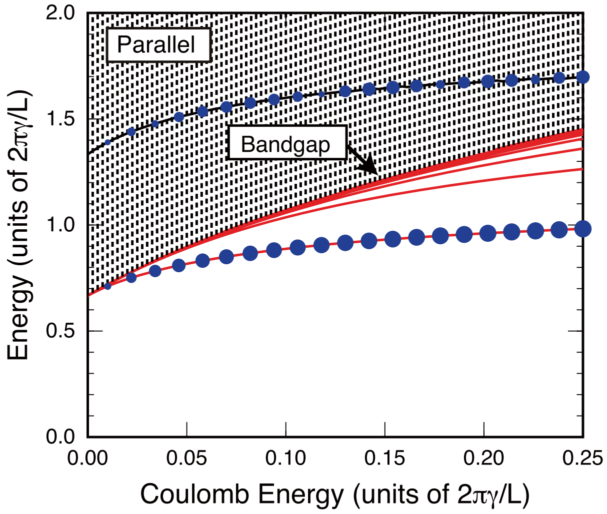

Figure 7. Energy levels of exciton with parallel polarization as a function of effective strength of the Coulomb energy v. Red lines below the bandgap denote bound excitons. Dotted region above the bandgap denotes continuous levels of scattering e–h pairs. Blue closed circles denote appreciable oscillator strength; the magnitude is proportional to the radius. The solid line in the dotted region denotes the exciton level, which consists mainly of an electron in the second-lowest conduction band and a hole in the second-highest valence band.

In the $\boldsymbol{k}\cdot\boldsymbol{p}$ scheme, all physical quantities become universal if the length and energy are scaled by L and $2\pi\gamma/L$, respectively. The strength of the Coulomb interaction in a SWNT is characterized by the dimensionless quantity given by the ratio of the typical Coulomb energy $e^2/\kappa L$ and the typical kinetic energy $2\pi\gamma/L$, i.e.

$$v \equiv \frac{e^2}{\kappa L}\frac{L}{2\pi\gamma} \approx \frac{0.35}{\kappa}. \qquad (58)$$

The typical strength of the Coulomb energy is of the order of 0.1–0.2 when κ is chosen around $\kappa = 2.4$ for graphite. In the following calculations, the cutoff energy $\varepsilon_{\mathrm{c}}/(2\pi\gamma/L) = 10$ in equation (50) is chosen. This cutoff energy corresponds to half of the π bandwidth for a SWNT having a diameter of ~1.4 nm. The parameter α_{c}, which represents the smoothness of the cutoff, is set to $\alpha_{\mathrm{c}} = 4$.

Figure 7 shows the energy levels of exciton states with parallel polarization as a function of the effective strength of the Coulomb energy v. Scattering e–h pairs exist in the dotted region above the bandgap. Because of the self-energy due to the Coulomb interaction, the band edges of the lowest conduction and highest valence bands shift to higher- and lower-energy sides, respectively. Consequently, the bandgap increases with the Coulomb energy. Well-defined exciton states, which are denoted by red lines, lie below the bandgap. The binding energies of the excitons, which are represented by the energy differences between the bandgap and the exciton levels, increase with the Coulomb energy. However, the energy level of the exciton increases with the Coulomb energy because the increase in the bandgap exceeds the decrease in the binding energy. The number of exciton states increases with the Coulomb energy. The discrete levels correspond to those of a hydrogen-like atom consisting of an electron and a hole, i.e. bound excitons.

The oscillator strength is proportional to $|\int \mathrm{d}\boldsymbol{r} \langle u, l|\hat{\boldsymbol{j}}(\boldsymbol{r})|g\rangle|^2/\varepsilon^l_u$. The appreciable oscillator strength is denoted by blue dots whose radii are proportional to the oscillator strength. The oscillator strength is concentrated on the lowest exciton, which is in the even-parity state (see the introduction of section 4). The even-parity states exhibit the allowed optical transitions. The third-lowest and fifth-lowest excitons are also even-parity states. However, these higher even-parity states have extremely small oscillator strengths. In the region of the scattering e–h pair states, a level with appreciable oscillator strength exists. This state is an even-parity bound exciton consisting mainly of an electron in the second-lowest conduction band and a hole in the second-highest valence band.

4.6. Perpendicular polarization

Perpendicularly polarized excitons are also calculated using the screened Hartree–Fock approximation (51) [86]. Because of the Fourier component (31) of perpendicular polarization, exciton states with $l = \pm 1$ in equation (37) are excited. The excitation energy for $l = +1$ is the same as that for $l = -1$ (see figure 6) when e–h band asymmetry is neglected (see section 2.3.3). Here, we ignore the e–h band asymmetry, and exciton states with $l = +1$ or -1 are degenerate. The effect of the e–h band asymmetry shall be considered in section 6.4.

For perpendicular polarization, the long-range e–h EXI $A^{\mathrm{EXI}}_{uu',l}(\omega)$ or depolarization field arises. In the absence of the e–h EXI, those excitons are degenerate. However, $A^{\mathrm{EXI}}_{uu',l}(\omega)$ gives rise to a large level splitting between $^1|\mathrm{KK} - \mathrm{K}'\mathrm{K}'(+)\rangle$ and $^1|\mathrm{KK} - \mathrm{K}'\mathrm{K}'(-)\rangle$ excitons. Because the matrix elements of the induced current $\langle u, l|\hat{\boldsymbol{j}}(\boldsymbol{r})|g\rangle$ are identical for the K and K′ valleys, the matrix element of the induced current for the $^1|\mathrm{KK} - \mathrm{K}'\mathrm{K}'(-)\rangle$ exciton becomes zero owing to the perfect cancellation between the induced currents of $^1|\mathrm{KK}\rangle$ and $^1|\mathrm{K}'\mathrm{K}'\rangle$. Therefore, the $^1|\mathrm{KK} - \mathrm{K}'\mathrm{K}'(-)\rangle$ exciton is optically forbidden, i.e. a dark exciton. In addition, the e–h EXI becomes zero, as determined by equation (52). On the other hand, the $^1|\mathrm{KK} - \mathrm{K}'\mathrm{K}'(+)\rangle$ exciton has a finite induced current, i.e. it is a bright exciton whose energy shifts upward due to the e–h EXI.

The wavefunction ψ^l_Λ for the bright $^1|\mathrm{KK} - \mathrm{K}'\mathrm{K}'(+)\rangle$ exciton for perpendicular polarization can be expanded by the exciton wavefunction ϕ^l_u excluding the e–h EXI as

$$\psi^l_\Lambda = \sum_u \alpha^l_{\Lambda,u}\phi^l_u, \tag{59}$$

where $\alpha^l_{\Lambda,u}$ represents the expansion coefficients. The equations for $\alpha^l_{\Lambda,u}$ are given by

$$\sum_{u'}[\varepsilon_u\delta_{uu'} + A^{\mathrm{EXI}}_{uu',l}(\omega)]\alpha^l_{\Lambda,u'} = \hbar\omega\alpha^l_{\Lambda,u}. \tag{60}$$

Because of the frequency dependence of the dynamical e–h EXI, equation (60) has a nonlinear form. For an exciton confined in a highly symmetric structure such as a sphere, cylinder or slab, the nonlinear equation can be solved by using a bisection method [78].

The envelope functions of the electron and the hole in a SWNT are proportional to a plane wave, as shown in equation (12). When the direction of light is perpendicular to the tube axis, the wavenumber of the exciton in the axial direction becomes zero. Thus, the matrix element of the induced current in the K and K′ valleys is written as $\langle g|\hat{j}_x(\boldsymbol{r})|u, l\rangle = \frac{1}{\sqrt{AL}} j^l_u \exp(\mathrm{i}l\theta)$, where A and L are the lengths in the axial and circumferential directions, respectively. The Green function G^L_{xx} for a SWNT can be extracted by taking the limit $\omega/c \to 0$ in the Green function for a hollow cylindrical shape [87]. Because the radius of a SWNT is much smaller than the wavelength of light, G^L_{xx} is well approximated as

$$G^L_{xx}(\boldsymbol{r}, \boldsymbol{r}') = -\mathrm{i}\frac{4\pi^2}{\omega\kappa}\frac{1}{AL^2}\sum_n\sum_k(-1)^{n+1}|n| \times \mathrm{e}^{\mathrm{i}k(y-y')}\mathrm{e}^{\mathrm{i}n(\theta-\theta')}, \tag{61}$$

where k is the wavenumber along the axis and n is an integer. Then, the e–h EXI is obtained as $A^{\mathrm{EXI}}_{uu';l}(\omega) = (-1)^{l+1}|l|(4\pi^2\hbar/\kappa L\omega)(j^{l*}_u j^l_{u'}/\varepsilon^l_{u'})$. The dynamical e–h EXI has a finite value for perpendicular polarization ($l = \pm 1$). In the following, the explicitly l-dependent factor $(-1)^{l+1}|l|$ is replaced by 1 because $l = \pm 1$. Thus, the equations for the expansion coefficients $\alpha^l_{\Lambda,u}$ are written as

$$\sum_{u'}\left[\varepsilon^l_u\delta_{uu'} + \hbar\frac{4\pi^2}{\kappa L\omega}\frac{j^{l*}_u j^l_{u'}}{\varepsilon^l_{u'}}\right]\alpha^l_{\Lambda,u'} = \hbar\omega\alpha^l_{\Lambda,u}. \tag{62}$$

These nonlinear equations are rewritten as

$$\left[1 + \hbar^2\frac{4\pi^2}{\kappa L}\sum_u\frac{|j^l_u|^2}{\hbar\omega\varepsilon^l_u(\varepsilon^l_u - \hbar\omega)}\right]W^l_\Lambda = 0, \tag{63}$$

where $W^l_\Lambda = \sum_u j^l_u\alpha^l_{\Lambda,u}/\varepsilon^l_u$. Note that this transformation is possible because of the separable form of the dynamical e–h EXI with respect to index u. This separability appears for highly symmetric exciton confinement geometries. The energies of the exciton E^l_Λ in the dynamical e–h EXI are obtained as $\hbar\omega$ satisfying

$$G(\hbar\omega) = 1 + \hbar^2\frac{4\pi^2}{\kappa L}\sum_u\frac{|j^l_u|^2}{\hbar\omega\varepsilon^l_u(\varepsilon^l_u - \hbar\omega)} = 0. \tag{64}$$

Figure 8 shows $G(\hbar\omega)$ for perpendicularly polarized excitons in a SWNT with the effective strength of the Coulomb energy $v = 0.2$. The vertical dotted lines indicate the exciton energy ε^l_u without the dynamical e–h EXI, which corresponds to the energy of a dark exciton because the e–h EXI does not appear for the dark exciton due to the fact that $j^l_u = 0$ (see equation (62)). In figure 8, ε^l_u is calculated in the $\boldsymbol{k}\cdot\boldsymbol{p}$ scheme with the screened Hartree–Fock approximation (see section 4.2) [68]. Note that two types of dark excitons exist. One is odd-parity excitons (2p, 3p, etc), whose oscillator strength or j^l_u becomes zero for each K and K′ valley. For this

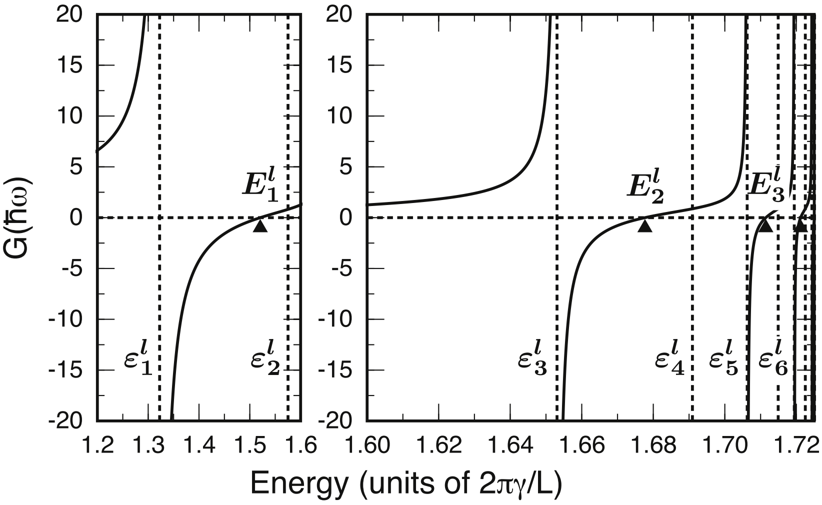

Figure 8. $G(\hbar\omega)$ (solid lines) and ε^l_u (vertical dotted lines). Exciton energies E^l_Λ with the dynamical e–h EXI are indicated by solid triangles.

type of dark state ($u = 2, 4, 6$, etc), $G(\hbar\omega)$ has no singularity at $\hbar\omega = \varepsilon^l_u$. The other type of dark state is the anti-bonding states $^1|\mathrm{KK} - \mathrm{K'K'}(-)\rangle$ consisting of even-parity excitons (1s, 2s, etc). In this case, j^l_u has finite values. When the asymmetry between the conduction and valence bands is neglected, $^1|\mathrm{KK}\rangle$ and $^1|\mathrm{K'K'}\rangle$ are degenerate. Therefore, the current density of $^1|\mathrm{KK} - \mathrm{K'K'}(-)\rangle$ is obtained by subtracting the current densities in the K and K′ valleys (see equation (57)), so these contributions are cancelled out, i.e. the current density of $^1|\mathrm{KK} - \mathrm{K'K'}(-)\rangle$ becomes zero. In this section, the band asymmetry is neglected. Since each j^l_u for even-parity excitons ($u = 1, 3, 5$, etc) has finite value, $G(\hbar\omega)$ diverges at $\hbar\omega = \varepsilon^l_u$.

The exciton energies E^l_Λ for bright $^1|\mathrm{KK} + \mathrm{K'K'}(+)\rangle$ excitons are obtained as the crossing points of $G(\hbar\omega)$ and the horizontal dotted line. $G(\hbar\omega)$ increases monotonically from $-\infty$ to ∞ between the divergent points at ε^l_u ($u = 1, 3$, etc). Therefore, all values of E^l_Λ can be obtained by using the bisection method. The calculated E^l_Λ values are indicated by solid triangles.

Figure 9 shows the energy levels of exciton states with perpendicular polarization as a function of the effective strength of the Coulomb energy v. Scattering e–h pairs exist in the dotted region above the bandgap. Bound exciton levels of $^1|\mathrm{KK} - \mathrm{K'K'}(+)\rangle$ are calculated from the bisection method in figure 8 and denoted by red solid lines. The bound exciton levels of $^1|\mathrm{KK} - \mathrm{K'K'}(-)\rangle$, consisting of even-parity excitons with energy ε^l_u ($u = 1, 3$, etc) and odd-parity excitons with energy ε^l_u ($u = 2, 4$, etc) are denoted by green solid and green dotted lines, respectively. The oscillator strengths of the lowest state $^1|\mathrm{KK} - \mathrm{K'K'}(+)\rangle$ are denoted by blue dots whose radii are proportional to the oscillator strength. The oscillator strengths are plotted in the same units as that in figure 7 but the magnitude is multiplied by 4. The oscillator strength for perpendicular polarization is about eight times smaller than that for parallel polarization because of the e–h EXI or depolarization effect.

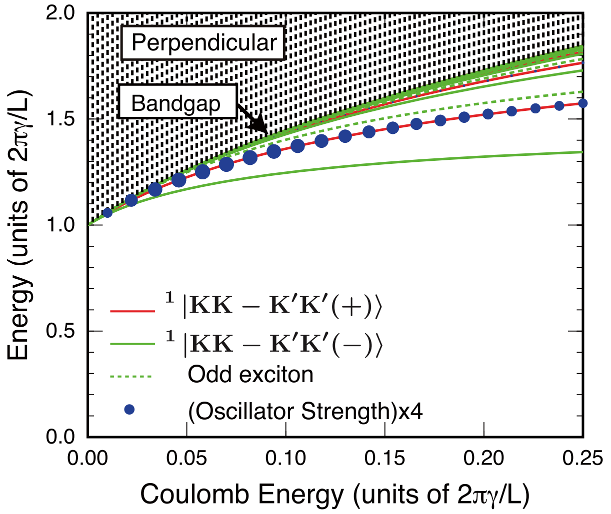

Figure 9. Energy levels of exciton with perpendicular polarization as a function of the effective strength of the Coulomb energy v. Red solid lines below the bandgap denote bound exciton levels of $^1|\mathrm{KK} - \mathrm{K'K'}(+)\rangle$. Green solid and green dotted lines denote bound exciton levels of $^1|\mathrm{KK} - \mathrm{K'K'}(-)\rangle$ consisting of even-parity excitons with energy ε^l_u ($u = 1, 3$, etc) and odd-parity excitons with energy ε^l_u ($u = 2, 4$, etc), respectively. The dotted region above the bandgap denotes continuous levels of scattering e–h pairs. Blue closed circles denote the appreciable oscillator strength; the magnitude is proportional to the radius.

The expansion coefficients $\alpha^l_{\Lambda,u}$ of the wavefunction ψ^l_Λ including the dynamical e–h EXI are obtained from equation (62) as

$$\alpha^l_{\Lambda,u} = -\frac{j^{l*}_u}{\varepsilon^l_u - E^l_\Lambda} \Bigg/ \sqrt{\sum_u \frac{|j^l_u|^2}{(\varepsilon^l_u - E^l_\Lambda)^2}}. \qquad (65)$$

Figure 10 shows $|\alpha^l_{\Lambda,u}|^2$ for the lowest ($\Lambda = 1$), the second-lowest ($\Lambda = 2$) and the third-lowest ($\Lambda = 3$) levels. Some coefficients $\alpha^l_{\Lambda,u}$ are zero for levels with odd-parity exciton with $u = 2, 4$, etc. These states have $j^l_u = 0$ in each K and K′ valleys; as a result, they cannot be involved via the dynamical e–h EXI.

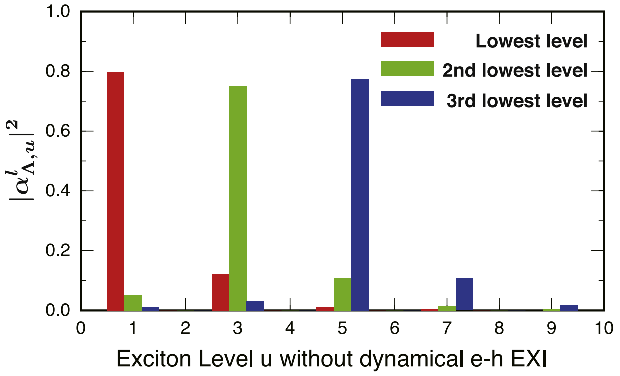

Figure 10. $|\alpha^l_{\Lambda,u}|$ of the wavefunction for the lowest (red bars), second-lowest (green bars) and third-lowest (blue bars) excitons.

5. Exciton–photon interaction

The interaction $H_{\mathrm{ex-ph}}$ between exciton $|\Lambda, l\rangle$ and the electromagnetic (EM) field is given by

$$H_{\mathrm{ex-ph}} \propto \int \mathrm{d}\boldsymbol{r}\, \langle \Lambda, l|\hat{\boldsymbol{j}}(\boldsymbol{r})|g\rangle \cdot \boldsymbol{E}(\boldsymbol{r}). \tag{66}$$

$\boldsymbol{E}(\boldsymbol{r})$ is usually considered as the applied EM field. However, the current density $\langle \Lambda, l|\hat{\boldsymbol{j}}(\boldsymbol{r})|g\rangle$ induced by the applied EM field generates a scattered field. Both the applied and scattered EM fields contribute to the current density, i.e. the EM field $\boldsymbol{E}(\boldsymbol{r})$ contains the scattered field. Therefore, the EM field and induced current density should be determined self-consistently. Here, we treat these fields self-consistently by using a microscopic optical response theory [83, 88, 89]. This self-consistent calculation has three advantages: (i) the resulting fields include a radiative correction, i.e. a radiative decay width and radiative shift in the exciton energy, (ii) with respect to a radiation force, a scattering force related to the radiative decay rate can be calculated and (iii) a depolarization field, which appears for EM fields polarized perpendicular to the tube axis, is included in the self-consistent EM field. Because of advantage (iii), the optical response including the depolarization effect can be calculated in terms of $|u, l\rangle$ excluding the e–h EXI. I describe the self-consistent field calculation method in section 5.1. In section 5.2, I discuss the self-energy of excitons that appears in the self-consistent treatment.

5.1. Self-consistent formula

The generated EM field is expressed using the Green function for the Maxwell equations. In the original version of the microscopic optical response theory, the transverse component of the Green function should be extracted. Here, we use a revised version in which the full Green function can be used without splitting it into the transverse and longitudinal components [89]. Although the self-consistent method is applicable beyond the rotating-wave approximation (RWA), we apply the RWA in the following calculations. The current density due to the exciton is given by

$$\boldsymbol{j}(\boldsymbol{r}, \omega) = \int \mathrm{d}\boldsymbol{r}'\, \bar{\boldsymbol{\sigma}}(\boldsymbol{r}, \boldsymbol{r}') \cdot \boldsymbol{E}(\boldsymbol{r}', \omega), \tag{67}$$

where $\bar{\boldsymbol{\sigma}}$ is a conductivity tensor in the RWA:

$$\bar{\boldsymbol{\sigma}}(\boldsymbol{r}, \boldsymbol{r}') = \frac{\hbar}{\mathrm{i}} \sum_{u,l} \frac{1}{\varepsilon^l_u} \frac{\langle g|\hat{\boldsymbol{j}}(\boldsymbol{r})|u, l\rangle\langle u, l|\hat{\boldsymbol{j}}(\boldsymbol{r}')|g\rangle}{\varepsilon^l_u - \hbar\omega - \mathrm{i}\Gamma}. \tag{68}$$

The induced current density produces the scattered field. The total EM field is written as

$$\boldsymbol{E}(\boldsymbol{r}) = \boldsymbol{D}(\boldsymbol{r}) + \int \mathrm{d}\boldsymbol{r}'\, \bar{\boldsymbol{G}}(\boldsymbol{r}, \boldsymbol{r}') \cdot \boldsymbol{j}(\boldsymbol{r}'), \tag{69}$$

where $\boldsymbol{D}$ is an applied field and $\bar{\boldsymbol{G}}$ is a dyadic Green function for the Maxwell equations satisfying

$$\nabla \times \nabla \times \bar{\boldsymbol{G}}(\boldsymbol{r}, \boldsymbol{r}') - \kappa(\boldsymbol{r}) q_0^2 \bar{\boldsymbol{G}}(\boldsymbol{r}, \boldsymbol{r}') = \boldsymbol{I}\delta(\boldsymbol{r} - \boldsymbol{r}'), \tag{70}$$

where κ is the background dielectric constant, $q_0 = \omega/c$, and $\boldsymbol{I}$ is the identity tensor. The Green functions can be expressed analytically for simple inhomogeneous media such as single or multilayer structures of slabs, cylinders and spheres [90]. The dyadic Green function for a hollow cylindrical shape with a surrounding background dielectric constant κ is given by

$$\begin{aligned} G_{yy}(\boldsymbol{r}, \boldsymbol{r}') &= -\frac{q_0^2}{2\omega\kappa} \sum_{n=-\infty}^{\infty} \int_{-\infty}^{\infty} \mathrm{d}k_y (-1)^n J_n(qa) H^{(1)}_n(qa) \\ &\quad \times \mathrm{e}^{\mathrm{i}k_y(y-y')} \mathrm{e}^{\mathrm{i}n(\theta-\theta')}, \\ G_{xx}(\boldsymbol{r}, \boldsymbol{r}') &= -\frac{q_0^2}{8\omega\kappa} \sum_{n=-\infty}^{\infty} \int_{-\infty}^{\infty} \mathrm{d}k_y (-1)^{n+1} \\ &\quad \times [J_{n-1}(qa) - J_{n+1}(qa)] \\ &\quad \times [H^{(1)}_{n-1}(qa) - H^{(1)}_{n+1}(qa)] \mathrm{e}^{\mathrm{i}k_y(y-y')} \mathrm{e}^{\mathrm{i}n(\theta-\theta')}, \end{aligned} \tag{71}$$

where $q = \sqrt{\kappa} q_0$, a is the radius of the cylinder, θ is the azimuth, and $J_n(qa)$ and $H^{(1)}_n(qa)$ are the Bessel and Hankel functions of the first kind, respectively. Substituting equation (67) into (69), we obtain

$$\boldsymbol{E}(\boldsymbol{r}) = \boldsymbol{D}(\boldsymbol{r}) + \frac{\hbar}{\mathrm{i}} \sum_{u,l} \int \mathrm{d}\boldsymbol{r}'\, \bar{\boldsymbol{G}}(\boldsymbol{r}, \boldsymbol{r}') \cdot \frac{\langle g|\hat{\boldsymbol{j}}(\boldsymbol{r}')|u, l\rangle}{\varepsilon^l_u} X_{u,l}, \tag{72}$$

with

$$X_{u,l} = \frac{1}{\varepsilon^l_u - \hbar\omega - \mathrm{i}\Gamma} \int \mathrm{d}\boldsymbol{r}\, \langle u, l|\hat{\boldsymbol{j}}(\boldsymbol{r})|g\rangle \cdot \boldsymbol{E}(\boldsymbol{r}). \tag{73}$$

By multiplying $\langle u, l|\hat{\boldsymbol{j}}(\boldsymbol{r})|g\rangle$ from the left-hand side of equation (72) and integrating with respect to $\boldsymbol{r}$, the self-consistent equations for $X_{u,l}$ are derived as follows:

$$\sum_{u'} [(\varepsilon^l_u - \hbar\omega - \mathrm{i}\Gamma)\delta_{uu'} + A_{uu',l}] X_{u',l} = B^{(0)}_{u,l}, \tag{74}$$

with

$$A_{uu',l} = \frac{\mathrm{i}\hbar}{\varepsilon^l_{u'}} \int \mathrm{d}\boldsymbol{r} \int \mathrm{d}\boldsymbol{r}'\, \langle u, l|\hat{\boldsymbol{j}}(\boldsymbol{r})|g\rangle \cdot \bar{\boldsymbol{G}}(\boldsymbol{r}, \boldsymbol{r}') \cdot \langle g|\hat{\boldsymbol{j}}(\boldsymbol{r}')|u', l\rangle, \tag{75}$$

$$B^{(0)}_{u,l} = \int \mathrm{d}\boldsymbol{r}\, \langle u, l|\hat{\boldsymbol{j}}(\boldsymbol{r})|g\rangle \cdot \boldsymbol{D}(\boldsymbol{r}). \tag{76}$$

The factor $A_{uu',l}$ represents self-interaction of the induced current density via the EM field. Note that the dyadic Green function includes both transverse and longitudinal components. The interaction via the transverse EM field provides the radiative correction, whereas the longitudinal component provides the dynamical e–h EXI (52) [78]. We use $\kappa = 2.4$ for graphite in the evaluation of $A_{uu',l}$. For the other evaluation, the background dielectric constant is set to $\kappa = 1$ because the SWNTs are assumed to be surrounded by vacuum.

The self-consistently determined current density $\boldsymbol{j}_s(\boldsymbol{r})$ is written in terms of $X_{u,l}$ as follows:

$$\boldsymbol{j}_s(\boldsymbol{r}) = \frac{\hbar}{\mathrm{i}} \sum_{u,l} \frac{\langle g|\hat{\boldsymbol{j}}(\boldsymbol{r})|u,l\rangle}{\varepsilon_u^l} X_{u,l}. \qquad (77)$$

Substituting this into equation (69), we obtain the self-consistently determined EM field as follows:

$$\boldsymbol{E}(\boldsymbol{r}) = \boldsymbol{D}(\boldsymbol{r}) + \frac{\hbar}{\mathrm{i}} \sum_{u,l} \int \mathrm{d}\boldsymbol{r}'\, \bar{\boldsymbol{G}}(\boldsymbol{r},\boldsymbol{r}') \cdot \frac{\langle g|\hat{\boldsymbol{j}}(\boldsymbol{r}')|u,l\rangle}{\varepsilon_u^l} X_{u,l}. \qquad (78)$$

5.2. Self-energy of excitons

The self-energy becomes zero for dark excitons because of the absence of the induced current density. In this subsection, therefore, we focus on bright excitons. The energy $\tilde{E}_\Lambda^l$ including the self-energy via the EM field is obtained as the energy of a self-sustaining mode without the applied field $\boldsymbol{D}$, i.e. $B_{u,l}^{(0)} = 0$. From equation (74) without the damping energy Γ, $\tilde{E}_\Lambda^l$ can be obtained as the solutions $\hbar\omega$ of the following equations:

$$\sum_{u'} (\varepsilon_u^l \delta_{uu'} + A_{uu',l}) X_{u',l} = \hbar\omega X_{u,l}. \qquad (79)$$

These simultaneous equations have a nonlinear form because ω or q is included as an argument of the Bessel functions in the dyadic Green function through $A_{uu',l}$. The self-energy of the exciton via the EM field is calculated from $\Delta\tilde{E}_\Lambda^l \equiv \tilde{E}_\Lambda^l - \varepsilon_u^l \equiv \mathrm{Re}(\Delta\tilde{E}_\Lambda^l) - \mathrm{i}\Gamma_{\Lambda,l}^{\mathrm{rad}}$, where $\Gamma_{\Lambda,l}^{\mathrm{rad}} \equiv -\mathrm{Im}(\tilde{E}_\Lambda^l)$. Here, I summarize the definitions of E_Λ^l, $\tilde{E}_\Lambda^l$ and ε_u^l. E_Λ^l is defined as the exciton energy including the e–h EXI, whereas $\tilde{E}_\Lambda^l$ is defined as the exciton energy including both the e–h EXI (interaction via longitudinal field) and interaction via the transverse field. Thus, E_Λ^l is a real but $\tilde{E}_\Lambda^l$ is a complex in general. ε_u^l is defined as the exciton energy obtained excluding the e–h EXI and interaction via a transverse field. The subtraction $\Delta\tilde{E}_\Lambda^l = \tilde{E}_\Lambda^l - \varepsilon_u^l$ is performed for excitons having the same order of energy.

Figure 11(a) shows the self-energy $\mathrm{Re}(\Delta\tilde{E}_1^0)$ and $\Gamma_{1,0}^{\mathrm{rad}}$ of the lowest exciton for parallel polarization as a function of the effective strength of the Coulomb energy $v = (e^2/\kappa L)(2\pi\gamma/L)^{-1}$. These real and imaginary parts of the self-energy are obtained by solving simultaneous nonlinear equations (79) by using an iteration method. The energy on the right-hand vertical axis is evaluated for a SWNT with a diameter $d = 0.78$ nm. The intrinsic radiative decay width is ≈20 μeV for $v = 0.15$. This radiative width corresponds to an intrinsic radiative lifetime of ≈33 ps.

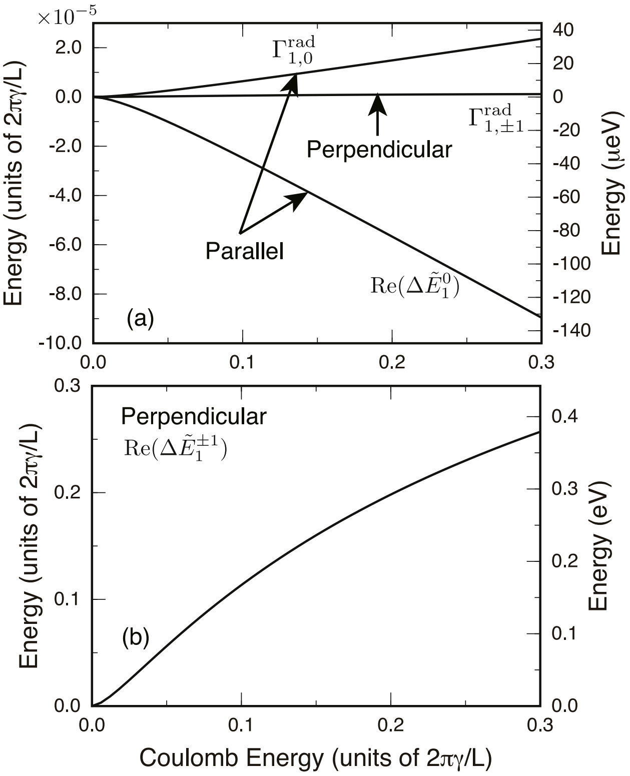

Figure 11. Self-energy of an exciton via the EM field as a function of the effective strength of the Coulomb energy v. The energy on the right-hand vertical axis is calculated for a SWNT with $d = 0.78$ nm. (a) Real $[\mathrm{Re}(\Delta\tilde{E}_1^0)]$ and imaginary $[\Gamma_{1,0}^{\mathrm{rad}} = -\mathrm{Im}(\Delta\tilde{E}_1^0)]$ parts of the self-energy of the lowest exciton for parallel polarization, and the imaginary part $[\Gamma_{1,\pm1}^{\mathrm{rad}} = -\mathrm{Im}(\Delta\tilde{E}_1^{\pm1})]$ of the self-energy of the lowest exciton for perpendicular polarization. (b) Real part $[\mathrm{Re}(\Delta\tilde{E}_1^{\pm1})]$ of the self-energy of the lowest exciton for perpendicular polarization. Reproduced with permission from [87]. Copyright 2009 American Physical Society.

The intrinsic radiative lifetime of a zigzag SWNT with $d = 0.78$ nm obtained by *ab initio* calculation was reported to be 19.1 ps [91]. The radiative lifetime in the present calculation is similar to that in the *ab initio* calculation. The effective radiative lifetime is longer than the intrinsic one because the exciton states are thermally distributed and a dark exciton exists. The enhancement factor of the effective radiative lifetime owing to thermalization is proportional to the square root of the temperature for a quantum wire [92] and this factor for a SWNT at room temperature is ≈100 [91]. The effect of a dark exciton on the effective lifetime depends on the level splitting of bright and dark states [91]. In a recent absorption experiment for SWNTs, the extrapolated level splitting was a few millielectronvolts (see section 6.3) [29, 30]. This level splitting enhances the effective radiative lifetime by a factor of 2.5. Consequently, in our calculation, the effective radiative lifetime is 8.3 ns. This value is in rough agreement with the experimental result of ∼10 ns for SWNTs with small diameters (between 0.76 and 0.91 nm) [93].

$\Gamma_{1,\pm1}^{\mathrm{rad}}$ and $\mathrm{Re}(\Delta\tilde{E}_1^{\pm1})$ for the lowest exciton for perpendicular polarization are shown in figures 11(a) and (b), respectively. The radiative decay width for $v = 0.15$ is about one-tenth of that for parallel polarization. This fact is understood in terms of the ratio of the oscillator strength between excitons for parallel and perpendicular polarization, as shown in figures 7 and 9, respectively. $\mathrm{Re}(\Delta\tilde{E}_1^{\pm1})$ exhibits quite a different order of magnitude compared to $\mathrm{Re}(\Delta\tilde{E}_1^0)$, $\Gamma_{1,0}^{\mathrm{rad}}$ and $\Gamma_{1,\pm1}^{\mathrm{rad}}$. For parallel polarization, the long-range e–h EXI does not appear; thus, $\mathrm{Re}(\Delta\tilde{E}_1^0)$ is the energy shift due to the exciton self-energy via the transverse EM field. For perpendicularly polarized excitons, the long-range e–h EXI appears, causing a large energy shift $\mathrm{Re}(\Delta\tilde{E}_1^{\pm1})$. This shift is called the depolarization shift because the long-range e–h EXI can be considered as the interaction between the exciton and its depolarization field [80–83]. This statement is easily confirmed by rewriting equation (52) as follows:

$$A_{uu',l}^{\mathrm{EXI}}(\omega) = \int \mathrm{d}\boldsymbol{r}\, \langle u, l|\hat{\boldsymbol{j}}(\boldsymbol{r})|g\rangle \cdot \boldsymbol{E}_{u',l}^{\mathrm{dep}}(\boldsymbol{r}), \tag{80}$$

where

$$\boldsymbol{E}_{u',l}^{\mathrm{dep}}(\boldsymbol{r}) = \frac{\mathrm{i}\hbar}{\varepsilon_{u'}^{l}} \int \mathrm{d}\boldsymbol{r}'\, \bar{\boldsymbol{G}}^{L}(\boldsymbol{r},\boldsymbol{r}') \cdot \langle g|\hat{\boldsymbol{j}}(\boldsymbol{r}')|u', l\rangle \tag{81}$$

is the depolarization field generated by the induced current $\langle g|\hat{\boldsymbol{j}}(\boldsymbol{r}')|u', l\rangle$ of the exciton.

6. Optical absorption

The optical absorption P per unit area is calculated as

$$P(\omega) = \frac{1}{2AL} \int \mathrm{d}\boldsymbol{r}\, \mathrm{Re}[\boldsymbol{j}_s^*(\boldsymbol{r},\omega) \cdot \boldsymbol{E}(\boldsymbol{r},\omega)], \tag{82}$$

where $\boldsymbol{j}_s$ and $\boldsymbol{E}$ are the self-consistently determined current density and EM field, respectively. Substituting equations (77) and (78) into equation (82), we express the absorption in the self-consistent treatment as follows:

$$P(\omega) = \frac{\hbar\Gamma}{2AL} \sum_{u,l} \frac{|X_{u,l}(\omega)|^2}{\varepsilon_u^l}. \tag{83}$$

If we neglect self-consistency, the absorption spectra are calculated as

$$P(\omega) = \frac{1}{2AL} \int \mathrm{d}\boldsymbol{r}\, \mathrm{Re}[\boldsymbol{j}^*(\boldsymbol{r},\omega) \cdot \boldsymbol{D}(\boldsymbol{r},\omega)], \tag{84}$$

where $\boldsymbol{j}$ is the current density given by equation (67) and $\boldsymbol{D}$ is the applied external field. The effect of the self-consistent field appears as the exciton self-energy, which produces a peak shift and an additional radiative width in the absorption spectra. For parallel polarized excitons, both the real and imaginary parts of the self-energy are a few tens of microelectronvolts (see figure 11(a)), which is much smaller than the exciton energy (≈1 eV). Thus, the self-consistent treatment is not important. For perpendicular polarization, however, the long-range e–h EXI arises and provides a large real part of the self-energy (a few hundreds of millielectronvolts) (see figure 11(b)). Therefore, the self-consistent treatment is necessary in order to calculate the absorption spectra for a perpendicularly polarized field.

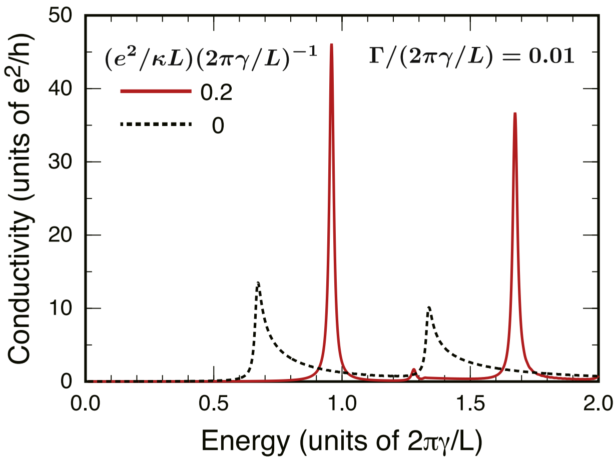

Figure 12. Calculated absorption spectra of a semiconducting SWNT for parallel polarization. The red solid line denotes the spectrum in the presence of the effective strength of the Coulomb energy $v = 0.2$; the dotted black line represents that in the absence of the interaction.

6.1. Parallel polarization

Figure 12 shows absorption spectra for the effective strength of the Coulomb energy $v = 0.2$ (red solid line) and 0 (dotted line), which are calculated without the self-consistent treatment. The phenomenological damping energy is $\Gamma = 0.01(2\pi\gamma/L)$. Compared with the spectrum in the absence of the Coulomb interaction (dotted line), the peak energies are shifted to higher energies and the peak intensities are enhanced by the exciton effect in the spectrum at $v = 0.2$ (red line) [68]. Figure 7 shows that the second-lowest peak of the red solid line corresponds to a bound exciton in the e–h continuum above the bandgap.

6.2. Perpendicular polarization

When the applied EM field is polarized perpendicular to the tube axis, the long-range e–h EXI or depolarization field arises because of the induced charge (depolarization charge), as depicted in figure 6. In addition to the applied field, the depolarization field contributes to the excitation of electronic states. Therefore, the self-consistent treatment is necessary, as described in the introduction of section 5, and the optical absorption can be calculated from equation (83) (method I). However, the self-consistent calculation has been performed in a different way so far (method II) [14, 86, 94–96]. The two different calculations provide almost the same results (see the blue dotted line and green open circles in figure 14(b)), but the effect of radiative damping of excitons is not included in self-consistent method II.

I briefly review the self-consistent method II. For the perpendicularly polarized external field given by equation (31), the self-consistently determined current density $j_{s,x}^l$ is induced in the circumferential direction. The corresponding induced charge density ρ_s^l is calculated as

$$\rho_s^l = \frac{2\pi}{L} \frac{l}{\omega} j_{s,x}^l \tag{85}$$

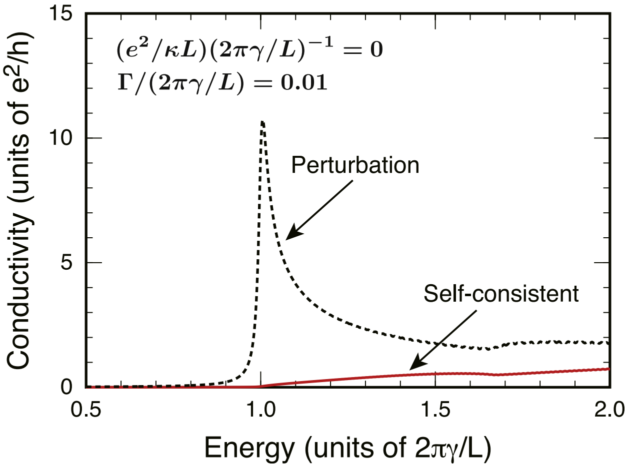

Figure 13. Calculated absorption spectra of a semiconducting SWNT for perpendicular polarization. Exciton effect is neglected. Red solid (dotted) line denotes spectrum with (without) the depolarization effect.

from the equation of continuity:

$$\frac{\partial}{\partial t}\rho_s^l e^{il\theta-i\omega t} + \frac{2\pi}{L}\frac{\partial}{\partial\theta} j_{s,x}^l e^{il\theta-i\omega t} = 0. \tag{86}$$

The potential $\phi(\theta,\theta')$ formed by a line charge along the axis direction at θ' with the density ρ_s^l is given at θ by

$$\phi(\theta,\theta') = -\frac{2\rho_s^l}{\kappa}\ln\left|\frac{L}{\pi}\sin\frac{\theta-\theta'}{2}\right|. \tag{87}$$

Then, the induced charge is found to produce the potential

$$\phi(\theta) = \frac{L}{2\pi}\int_0^{2\pi} d\theta'\phi(\theta,\theta') = \frac{L}{\kappa|l|}\rho_s^l e^{il\theta} \equiv \phi_s^l e^{il\theta}. \tag{88}$$

The potential gives rise to an electric field $-(2\pi/L)(\partial\phi/\partial\theta)$; therefore, the total electric field is obtained as

$$E_x^l = D_x^l - il\frac{2\pi}{L}\phi_s^l = D_x^l - i|l|\frac{4\pi^2}{\kappa L\omega} j_{s,x}^l. \tag{89}$$

By using $j_{s,x}^l = \sigma_{xx}^l E_x^l$ we obtain $E_x^l = D_x^l/\varepsilon_{xx}^l$, where

$$\varepsilon_{xx}^l = 1 + i|l|\frac{4\pi^2}{\kappa L\omega}\sigma_{xx}^l \tag{90}$$

is a dielectric function including the depolarization effect. Then, we have

$$j_{s,x}^l = \frac{\sigma_{xx}^l}{\varepsilon_{xx}^l} D_x^l. \tag{91}$$

Substituting equations (89) and (91) into equation (82), we have

$$P(\omega) = \frac{D^2}{8}\sum_{l=\pm1}\mathrm{Re}\left[\frac{\sigma_{xx}^l}{\varepsilon_{xx}^l}\right]. \tag{92}$$

Figure 13 shows the absorption spectra without the exciton effect. The red solid (dotted) line denotes the absorption calculated from equation (92) and (equation (84)), which includes (excludes) the depolarization effect. The peak in the dotted line around $1.0(2\pi\gamma/L)$ corresponds to the allowed transitions at the band edges. The peak disappears almost completely when the depolarization effect is included [14].

Next, we study absorption spectra including the Coulomb interaction. Figure 14(a) shows the absorption spectra of a semiconducting SWNT calculated including the exciton effect with the effective strength of the Coulomb energy $v = 0.2$. The red solid (dotted) line denotes absorption including (excluding) the depolarization effect, which is calculated from equation (92) and (equation (84)). When the depolarization effect is neglected, the peak due to the lowest exciton appears. When the depolarization effect is included, however, the peak is shifted towards the higher-energy side and its intensity is significantly reduced [86].

The e–h EXI can be interpreted as an interaction between the exciton and the depolarization field caused by the exciton as shown in equation (80). Because of the alternative description, two types of schemes can be used to calculate the optical spectra. In one, scheme (A), the exciton states are calculated including the dynamical e–h EXI. The induced current $\boldsymbol{j}$ is given by $\boldsymbol{j} = \bar{\boldsymbol{\sigma}}_{\mathrm{EXI}} \cdot \boldsymbol{D}$, where $\bar{\boldsymbol{\sigma}}_{\mathrm{EXI}}$ is the conductivity tensor (68) with $|u,l\rangle$ replaced by the exciton $|\Lambda,l\rangle$ including the dynamical e–h EXI. Then, the absorption is calculated from equation (84). In the other, scheme (B), the exciton states are obtained by excluding the e–h EXI. Instead, an actual applied field consisting of $\boldsymbol{D}$ and the depolarization field due to the exciton is determined self-consistently. In this case, the absorption is calculated from equation (83) (method I) or equation (92) (method II) [14, 86, 94–96]. Scheme (A) has more advantages than scheme (B) because exciton wavefunctions with e–h EXI cannot be obtained in scheme (B).

Figure 14(b) shows absorption spectra calculated by different methods. The red solid line denotes the absorption calculated by scheme (A) using equation (84) with $\boldsymbol{j} = \bar{\boldsymbol{\sigma}}_{\mathrm{EXI}} \cdot \boldsymbol{D}$. The blue dotted line and green open circles denote the absorption calculated by scheme (B) using equations (83) and (92), respectively. In equation (92), the self-interaction of excitons comes from the interaction between an exciton and its longitudinal depolarization field. In addition to the longitudinal component, the self-interaction of the exciton via the transverse EM field, or the radiative correction, is contained in equation (83). Therefore, these two spectra differ by the radiative damping. However, the radiative damping is quite small, as shown by the line labeled $\Gamma_{1,\pm1}^{\mathrm{rad}}$ in figure 11. As a result, these two spectra denoted by the blue dotted line and green open circles are almost the same. When we use the dynamical e–h EXI, the calculated absorption in scheme (A), denoted by the red solid line, agrees with that in scheme (B), denoted by the blue dotted line and green open circles. However, the conventional e–h EXI without the dynamical characteristics produces considerably different absorption, denoted by the red dashed line. Therefore, the dynamical nature of the e–h EXI is quite important for calculating the exciton states of a SWNT [78].

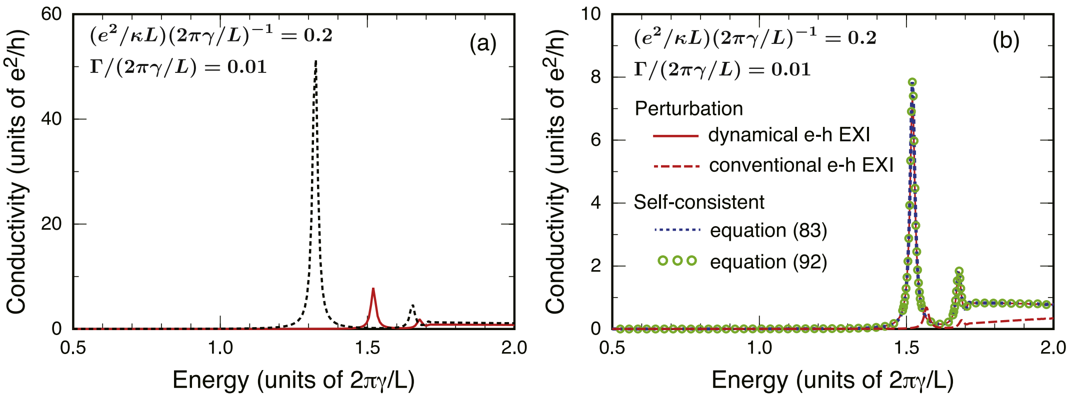

Figure 14. (a) Calculated absorption spectra of a semiconducting SWNT for perpendicular polarization. The exciton effect is included. The red solid (dotted) line denotes spectrum with (without) the dynamical e–h EXI or depolarization effect. (b) Absorption spectra calculated from exciton states with dynamical e–h EXI (red solid line), with conventional e–h EXI (red dashed line), self-consistent method with equation (83) (blue dotted line) and self-consistent method with equation (92) (green open circles).

6.3. Aharonov–Bohm effect in excitons

Optical spectroscopy is a powerful tool for studying excited states. In the optical spectra of SWNTs, the AB effect in SWNTs has been observed as the splitting of the spectral peaks of excitons [27, 29, 30]. The bandgaps in the K and K′ valleys are degenerate at $1.0(4\pi\gamma/3L)$, as shown in figure 4. In the presence of an AB flux passing through the tube axis, the degeneracy is symmetrically lifted upward and downward. The exciton states exhibit similar behavior. Namely, the bright $^1|\mathrm{KK} - \mathrm{K'K'}(+)\rangle$ and dark $^1|\mathrm{KK} - \mathrm{K'K'}(-)\rangle$ excitons for parallel polarization are almost degenerate (the level separation between them is a few millielectronvolts). When an AB flux is applied, the two almost degenerate excitons split symmetrically upwards and downwards with approaching to bright $^1|\mathrm{KK}\rangle$ and $^1|\mathrm{K'K'}\rangle$ excitons in a high magnetic field limit [84]. Thus, the dark $^1|\mathrm{KK} - \mathrm{K'K'}(-)\rangle$ exciton acquires a finite oscillator strength in the presence of the AB flux [84]. Therefore, this level splitting due to the AB effect can be observed by optical spectroscopy. In fact, this behavior has been observed in absorption [27, 28, 30] and PL spectra [27–29].

Zaric *et al* reported the first observation of the AB effect in optical spectra [27, 28]. Figure 15(a) shows the magnetic field dependence of the absorption spectra for a sample consisting of SWNTs 0.6–1.3 nm in diameter suspended in sodium cholate and heavy water. The light was linearly polarized along the magnetic field direction. Because SWNTs have a strong tendency to align in the direction of a magnetic field [20–23], the absorption increases with the magnetic field. The tendency to align arises from the large diamagnetic susceptibility in a magnetic field perpendicular to the tube axis [24–26]. At fields above ∼55 T, each of these peaks splits into two clearly resolved peaks due to the AB effect. Figure 15(b) shows the absorption spectra (solid lines) at 0 and 67 T for parallel and perpendicular polarizations. The dashed lines denote theoretical results. The absorption increases (decreases) with the magnetic field for parallel (perpendicular) polarization, and the splits appear only in the parallel case.

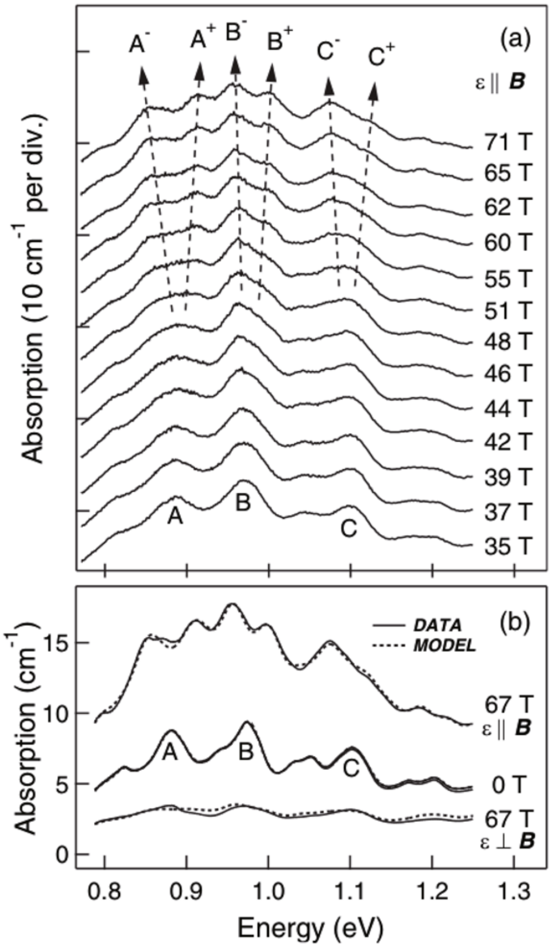

Figure 15. Absorption spectra of semiconducting SWNTs in a high magnetic field for (a) polarization parallel to the magnetic field (traces are offset) and (b) both polarizations (no intentional offset). Dotted lines in (b) are the calculated absorption [28]. Reproduced with permission from [28]. Copyright 2006 American Physical Society.

Note that level splitting does not seem to become observable until the magnetic field reaches a certain critical value and then starts to increase with the field. This

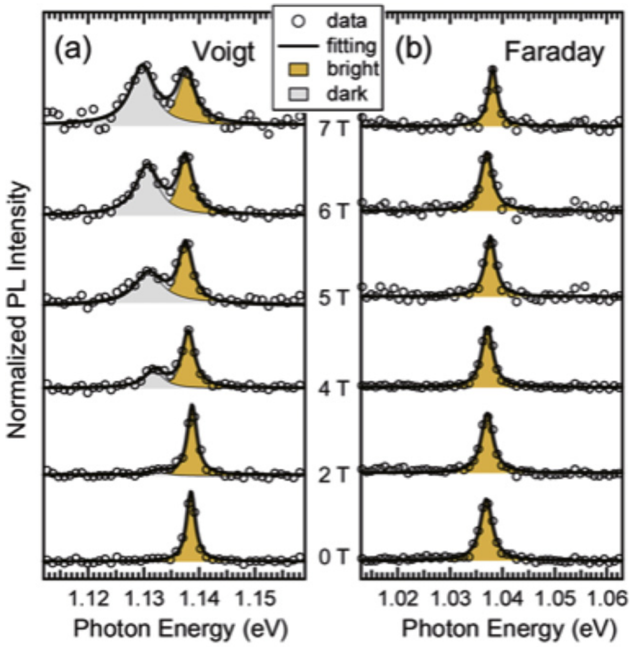

Figure 16. (a) Normalized PL spectra of a single $(n_1, n_2) = (9, 4)$ SWNT at 20 K in a magnetic field parallel to the tube axis. (b) Normalized PL spectra of a single $(n_1, n_2) = (9, 5)$ SWNT at 20 K in a magnetic field perpendicular to the tube axis [29]. Reproduced with permission from [29]. Copyright 2008 American Physical Society.

characteristic feature arises from the existence of the dark exciton ${}^1|\mathrm{KK} - \mathrm{K'K'}(-)\rangle$ close to the bright exciton ${}^1|\mathrm{KK} - \mathrm{K'K'}(+)\rangle$ [84]. The two peaks appear at a high magnetic field only when the AB splitting exceeds the splitting energy between the bright and dark states. This feature has been observed clearly by micro-PL spectroscopy of a single SWNT at low temperatures [29]. Figure 16(a) shows the normalized PL spectra of a single $(n_1, n_2) = (9, 4)$ SWNT under a magnetic field parallel to the tube axis. A single sharp PL peak originating from bright exciton recombination appears at zero magnetic field. With increasing magnetic field, an additional peak is clearly observed below the bright exciton peak. The additional peak can be considered as a brightening of the dark exciton ${}^1|\mathrm{KK} - \mathrm{K'K'}(-)\rangle$ due to the magnetic field. The energy level of the dark exciton is lower than that of the bright exciton. Figure 16(b) shows the results of similar experiments on a single $(n_1, n_2) = (9, 5)$ SWNT, in which the magnetic field is perpendicular to the tube axis. No spectral splitting induced by the magnetic field is observed even under a magnetic field of 7 T. Because the PL peak is split only under a parallel magnetic field, this splitting is attributed to the AB effect.

In figure 16(a), the lower PL peak shifts downwards, but the higher one does not change its position with increasing magnetic field. This behavior differs from the theoretical prediction, which is that almost-degenerate exciton levels of ${}^1|\mathrm{KK} - \mathrm{K'K'}(\pm)\rangle$ shift symmetrically downwards and upwards, respectively [84]. This is presumably because of the existence of impurities or trapping states having energies similar to the exciton energy in the absence of a magnetic field. In this case, the upper level exciton would decay nonradiatively to the trapping states, which would then emit a photon. The unwanted signal coming from the extra process can be avoided by using absorption spectroscopy. In fact, symmetric shifts in the absorption peaks are observed in figure 15.

The fine level splitting Δ_x between bright ${}^1|\mathrm{KK} - \mathrm{K'K'}(+)\rangle$ and dark ${}^1|\mathrm{KK} - \mathrm{K'K'}(-)\rangle$ excitons under parallel polarization was recently estimated from the absorption spectra under a strong magnetic field. A simple two-band model was introduced to analyze experimental data [98]. In this model, two excitons, ${}^1|\mathrm{KK}\rangle$ and ${}^1|\mathrm{K'K'}\rangle$, interact with each other with an energy Δ_x due to the short-range Coulomb interaction. The Hamiltonian in the two-band model is given by

$$H = \begin{array}{c} \begin{array}{cc} {}^1|\mathrm{KK}\rangle & \quad {}^1|\mathrm{K'K'}\rangle \end{array} \\ \begin{pmatrix} \varepsilon_0 - \Delta_{\mathrm{AB}}/2 & \Delta_x/2 \\ \Delta_x/2 & \varepsilon_0 + \Delta_{\mathrm{AB}}/2 \end{pmatrix} \end{array}, \qquad (93)$$

where ε_0 is the degenerate exciton energy in the K and K′ valleys in the absence of Δ_x and $\Delta_{\mathrm{AB}}(B) = \mu\phi$, where μ is a constant representing the level splitting between the excitons in the K and K′ valleys due to the AB flux ϕ. The energies are calculated from this Hamiltonian as $\varepsilon_\pm = \varepsilon_0 \pm \sqrt{\Delta_x^2 + \Delta_{\mathrm{AB}}^2}/2$. Therefore, the energy difference $\Delta(B)$ between two excitons under a magnetic field can be obtained as

$$\Delta(B) = \sqrt{\Delta_x^2 + \Delta_{\mathrm{AB}}^2}. \qquad (94)$$

The relative oscillator strengths are calculated as

$$I_\pm = \frac{1}{2} \pm \frac{1}{2} \frac{\Delta_x}{\sqrt{\Delta_x^2 + \Delta_{\mathrm{AB}}^2(B)}}, \qquad (95)$$

where the upper and lower signs represent the oscillator strengths for excitons having ε_+ and ε_-, respectively. For $\Delta_x > 0$, the exciton having ε_+ (ε_-) is in the bright (dark) state in the absence of the AB flux, and the situation is the opposite for $\Delta_x < 0$. We can determine μ and Δ_{AB} from the optical spectra by fitting the peak positions and relative intensities using equations (94) and (95).

Figure 17 shows the peak splitting and normalized absorption intensities as a function of the effective magnetic field B_{eff} for $(n_1, n_2) = (7, 5)$ SWNTs dispersed in a liquid [30]. Because the samples are ensembles of SWNTs, B_{eff} is corrected to include the contributions of all the randomly oriented SWNTs with respect to the mean orientation induced by the external magnetic field. The correction is estimated from a simulation of the spectrum convolution, assuming that the peak intensity is proportional to $\sin\delta$ when the tube axis is tilted by an angle δ from the magnetic field direction. The dashed lines were fitted using equations (94) and (95). The values of the splitting energy Δ_x between bright and dark excitons in the absence of a magnetic field obtained from the fitting is 6.8 meV and the coefficient μ, which determines the AB splitting in a magnetic field, is given by 0.73 meV T^{-1}. The coefficient $\mu = 2\Delta\varepsilon_{\mathrm{G}}$ for $(n_1, n_2) = (7, 5)$ SWNTs 0.83 nm in diameter is calculated as 0.81 meV T from equation (16).

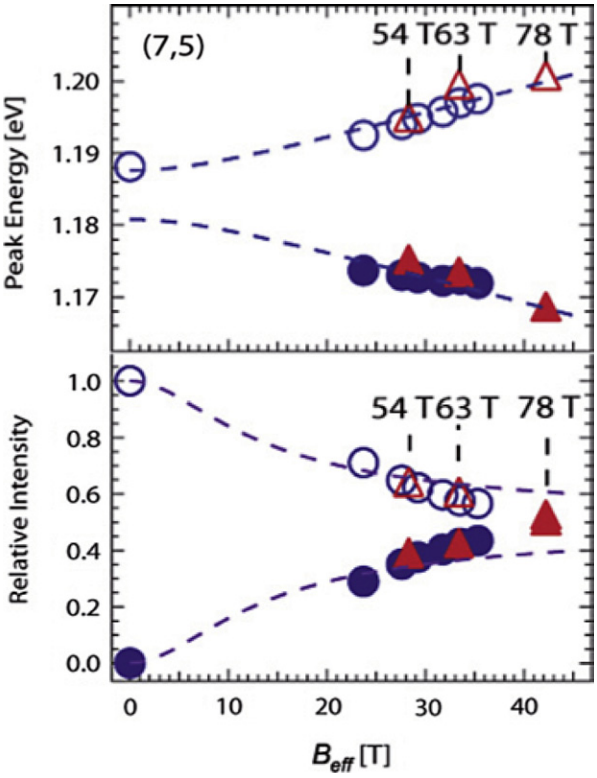

Figure 17. Change in the absorption and normalized intensity of spectral peaks for $(n_1, n_2) = (7, 5)$ SWNTs plotted against the effective magnetic field. Circles (triangles) denote results obtained from the nondestructive pulse magnet (destructive giant single-turn coil method [97]). Dashed lines are fitted using equations (94) and (95) [30]. Reproduced with permission from [30]. Copyright 2011 American Physical Society.

6.4. *Quasi-dark states*

In the above calculations, we ignored higher-order corrections in the $\boldsymbol{k}\cdot\boldsymbol{p}$ equation. In this case, the valence and conduction bands are symmetric with respect to the Fermi energy. Let us consider excitation with $l = +1$ of a SWNT with $\nu = +1$ for perpendicularly polarized light. Excitation from the $n = 0$ ($n = -1$) valence band to the $n = +1$ ($n = 0$) conduction band becomes allowed and in the K(K′) valley (see the middle and right panels in figure 6(b)). The two corresponding exciton states in the K and K′ valleys are degenerate owing to the symmetry of the electron and hole bands. When we consider the effective overlap integral, the e–h symmetry is broken, as described in section 2.3.3. Thus, the degeneracy of the two excitons in the K and K′ valleys is lifted. These excitons interact with each other because of the long-range e–h EXI; consequently, the bright $^1|\mathrm{KK}-\mathrm{K'K'}(+)\rangle$ and dark $^1|\mathrm{KK}-\mathrm{K'K'}(-)\rangle$ states are formed. When the two excitons are degenerate, the dark state has no oscillator strength because the $^1|\mathrm{KK}\rangle$ and $^1|\mathrm{K'K'}\rangle$ components cancel perfectly (see equation (57)). However, the cancellation becomes incomplete in the presence of e–h band asymmetry, so the dark state $^1|\mathrm{KK}-\mathrm{K'K'}(+)\rangle$ acquires a finite oscillator strength as a quasi-dark exciton (see figure 19(a)).

Figure 18 shows PLE spectra of various (n_1, n_2) species for excitation perpendicular to the tube axis [85]. The higher- and lower-energy peaks originate from the bright $^1|\mathrm{KK}-\mathrm{K'K'}(+)\rangle$ and quasi-dark $^1|\mathrm{KK}-\mathrm{K'K'}(-)\rangle$ excitons, respectively. The peak intensities $I_T^{(-)}$ for the quasi-dark exciton depend strongly on (n_1, n_2). Compared with the peak intensities $I_T^{(+)}$ for the bright exciton, near-zigzag SWNTs (close to $(n_1, 0)$) tend to have larger $I_T^{(-)}$, whereas near-armchair SWNTs (close to (n_1, n_1)) tend to have smaller $I_T^{(-)}$. This chirality dependence of $I_T^{(\pm)}$ is the result of the higher-order corrections.

To clarify the relationship between the quasi-dark excitons and the e–h band asymmetry, we studied the absorption spectra of excitons excited by perpendicular polarization theoretically. The higher-order correction of the $\boldsymbol{k}\cdot\boldsymbol{p}$ approximation is included in the exciton calculations. Figure 19(a) shows the calculated absorption spectra of (8, 6) SWNTs with (effective overlap integral $S = 0.1$) and without ($S = 0$) e–h band asymmetry for the effective strength of the Coulomb energy $v = 0.19$ [85]. A small peak due to the quasi-dark exciton appears for $S = 0.1$ but not for $S = 0$ because of the symmetric electron and hole bands.

To determine the Coulomb energy v, the calculated energy difference Δ_T between bright and quasi-dark excitons

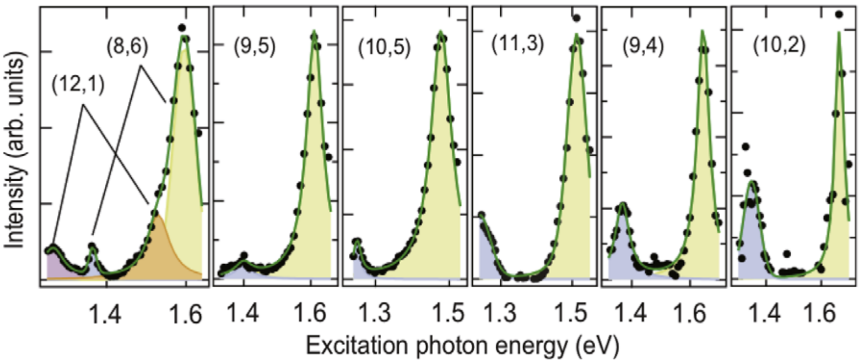

Figure 18. PLE spectra of various (n_1, n_2) species for excitation perpendicular to the tube axis. Higher- and lower-energy peaks come from the bright $^1|\mathrm{KK}-\mathrm{K'K'}(+)\rangle$ and quasi-dark $^1|\mathrm{KK}-\mathrm{K'K'}(-)\rangle$ excitons, respectively. Because the PL emission wavelength of (8, 6) and (12, 1) SWNTs are almost identical, the corresponding PLE spectra are combined. Reproduced with permission from [85]. Copyright 2010 American Physical Society.

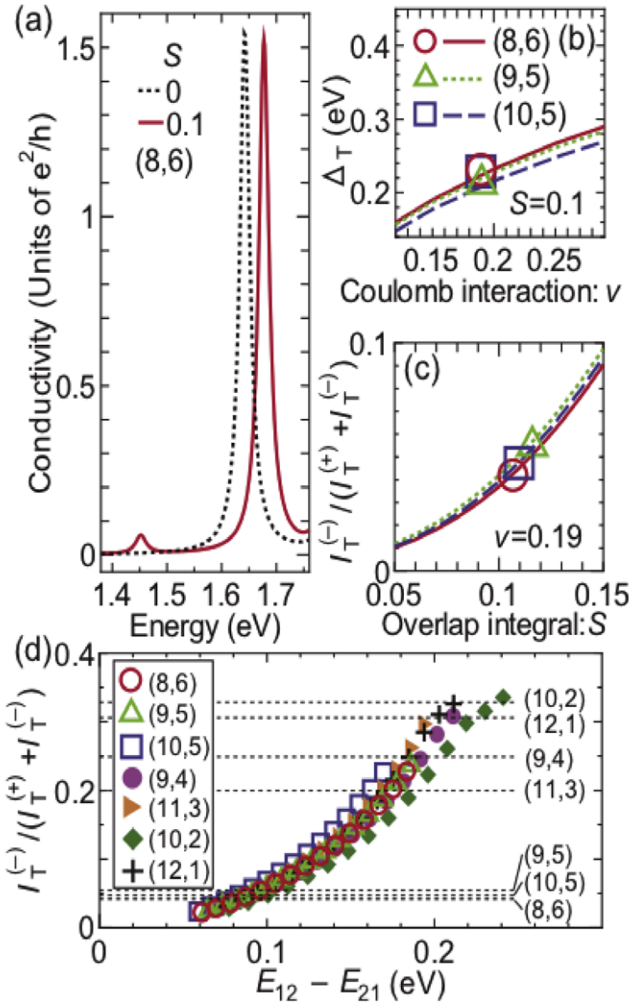

Figure 19. (a) Calculated absorption spectra of an (8, 6) SWNT with ($S = 0.1$) and without ($S = 0$) e–h band asymmetry. Small peak at 1.45 eV originates from the quasi-dark exciton $^1|\mathrm{KK} - \mathrm{K'K'}(-)\rangle$. (b) Energy splitting between bright and quasi-dark excitons for (8, 6), (9, 5) and (10, 5) SWNTs as a function of Coulomb energy v. Experimental data are denoted by open symbols. (c) Calculated quasi-dark exciton intensities normalized by the sum of bright and dark exciton intensities as a function of S. (d) Calculated normalized intensities of the quasi-dark excitons as a function of $E_{12} - E_{21}$. Experimental values are denoted by horizontal dashed lines. Reproduced with permission from [85]. Copyright 2010 American Physical Society.

is plotted in figure 19(b) for near-armchair SWNTs. The Δ_T value for near-armchair SWNTs is almost independent of S up to $S \sim 0.3$. Here, we choose $S = 0.1$. The experimentally observed Δ_T, which are indicated by open symbols, can be obtained for $v = 0.19$.

Figure 19(c) shows the calculated spectral intensity $I_T^{(-)}/(I_T^{(+)} + I_T^{(-)})$ of the quasi-dark excitons for near-armchair SWNTs as a function of S for $v = 0.19$. The curvature effect is small for these near-armchair SWNTs, so S is expected to be close to the value in graphene. We can evaluate $S \sim 0.1$ for the near-armchair SWNTs from the experimental data indicated by open symbols. This value of S is close to $S = 0.129$ which is conventionally used in the tight-binding model for graphene and SWNTs.

The $I_T^{(-)}/(I_T^{(+)} + I_T^{(-)})$ and $(E_{12} - E_{21})$ values of various (n_1, n_2) SWNTs were calculated for effective overlap integrals ranging from $0.08 \leq S \leq 0.22$ with a 0.01 step, where E_{12} and E_{21} are the lowest band-to-band excitation energy at the K and K′ points, respectively. $(E_{12} - E_{21})$ represents the degree of e–h band asymmetry and increases from 0 with increasing S. The symbols in figure 19(d) summarize the calculated $I_T^{(-)}/(I_T^{(+)} + I_T^{(-)})$ and $(E_{12} - E_{21})$ values. The plots for various (n_1, n_2) species lie on almost the same curve. This suggests that the spectral weight transfer $I_T^{(-)}/(I_T^{(+)} + I_T^{(-)})$ is characterized only by the degree of e–h band asymmetry. Horizontal dashed lines indicate the experimental values of $I_T^{(-)}/(I_T^{(+)} + I_T^{(-)})$ for each (n_1, n_2). Small-diameter near-zigzag SWNTs tend to have a large e–h band asymmetry. The corresponding effective overlap integral $S \sim 0.2$ is considerably larger than that of near-armchair SWNTs. This large chirality dependence of the effective overlap integral could be attributed to the change in the bond length due to the finite curvature. A more systematic theoretical study has also been reported [99].

7. Radiation force

In order to study the fundamental properties of SWNTs and develop applications, many researchers and industrial engineers strongly desire selective control of the spatial position of an individual SWNT and the selective sorting of SWNTs. The use of the resonant radiation force mediated by excitons is a promising technique for this purpose. The radiation force reflects the size quantization of exciton levels and changes significantly depending on geometric properties such as the size and shape of the target nano-object. Theoretically, this would enable us to selectively manipulate specific nano-objects [100, 101].

Well-defined SWNT excitons are observed in absorption and luminescence spectra even at room temperature. Owing to the steepness of the absorption peaks and the strong size dependence of the peak position, size-selective manipulation of SWNTs is possible. Furthermore, the optical spectra of SWNTs exhibit a strong polarization dependence (see sections 6.1 and 6.2). This strong anisotropy would be useful for manipulating and sorting SWNTs whose major axis is oriented parallel to the direction of light polarization.

The radiation force $\boldsymbol{F}$ exerted on a SWNT is calculated from a general expression [101, 102]:

$$\boldsymbol{F}(\omega) = \frac{1}{2}\mathrm{Re}\left\{\frac{\mathrm{i}}{\omega}\int \mathrm{d}\boldsymbol{r}\, [\nabla \boldsymbol{E}^*(\boldsymbol{r}, \omega)] \cdot \boldsymbol{j}_s(\boldsymbol{r}, \omega)\right\}, \qquad (96)$$

where $\boldsymbol{j}_s$ is the self-consistently determined induced current, which is given in equation (77). In the following calculations, the self-consistent field $\boldsymbol{E}$ including both the applied and scattered fields can be replaced by the applied field $\boldsymbol{D}$ because the contribution from the scattered field is cancelled out by the symmetry. This expression includes both dissipative (absorption and scattering) and gradient forces. When a propagating EM field is applied to an object, the dissipative force is exerted in the applied field direction by momentum transfer from a photon to the object. When the EM field intensity is spatially inhomogeneous, a gradient force is exerted on the SWNT. By using the gradient force, microscopic dielectric objects can be physically held and moved; this scientific instrument is called optical tweezers [103].

7.1. Dissipative force

First, we consider a situation in which a propagating plane EM field is applied to a SWNT. The EM field has a wavevector $\mathbf{q}$ perpendicular to the tube axis, whose direction is denoted by Z. The applied EM field is written as $\boldsymbol{D} = D\boldsymbol{e}\mathrm{e}^{\mathrm{i}qZ}$, where $\boldsymbol{e}$ represents unit polarization vectors. Consequently, the dissipative force $\boldsymbol{F}$ is exerted in the Z direction; it is expressed as [87]

$$F_Z(\omega) = \frac{\sqrt{\kappa}}{c} p(\omega) + \frac{\hbar}{2}\frac{\sqrt{\kappa}}{c}\sum_{uu'l}\frac{\mathrm{Im}(X_{u,l}A^*_{uu',l}X^*_{u',l})}{\varepsilon^l_u}, \qquad (97)$$

where $p(\omega) = ALP(\omega)$ is the total absorption and P is given in equation (83). The first and second terms on the right-hand side of equation (97) represent the absorption and scattering forces, respectively. The scattering force becomes zero if we neglect self-interaction. Therefore, the self-consistent treatment described in section 5.1 is necessary for evaluating the scattering force.

To study the characteristics of the dissipative force, we represent the expression of equation (97) by an individual exciton approximation, in which the self-interaction between different exciton states is neglected [87]. The self-interaction represented by a matrix can then be approximated by the scalar of the diagonal matrix elements, i.e. $A_{uu',l} = \delta_{uu'}A_{uu,l}$, and the exciton energy including the self-energy $\tilde{E}^l_\Lambda \approx \mathrm{Re}(\tilde{E}^l_u) - \mathrm{i}\Gamma^{\mathrm{rad}}_{u,l}$ is given by

$$\mathrm{Re}(\tilde{E}^l_u) = \varepsilon^l_u + \mathrm{Re}(A_{uu,l}), \qquad \Gamma^{\mathrm{rad}}_{u,l} = -\mathrm{Im}(A_{uu,l}). \quad (98)$$

Furthermore, the frequency dependence of $A_{uu,l}$ is neglected by setting $\hbar\omega = \varepsilon^l_u$. This approximation is valid when the self-interaction is much smaller than the separation of the exciton energies. The resulting expression for $F_Z(\omega)$ gives the spectral shape and indicates a clear dependence of the nonradiative decay width on the dissipative force. In this approximation, the dissipative force F_Z for parallel ($l = 0$) polarization is calculated as

$$F_Z(\omega) = 4\kappa A I_0 \sum_u \frac{\Gamma^{\mathrm{rad}}_{u,0}}{\varepsilon^0_u}\frac{\Gamma + \Gamma^{\mathrm{rad}}_{u,0}}{[\mathrm{Re}(\tilde{E}^0_u) - \hbar\omega]^2 + (\Gamma + \Gamma^{\mathrm{rad}}_{u,0})^2}, \qquad (99)$$

where $I_0 \equiv \sqrt{\kappa}cD^2/(8\pi)$ is the applied field intensity. The dissipative force spectra have a Lorentzian lineshape. $\mathrm{Re}(\tilde{E}^0_u)$ and $\Gamma^{\mathrm{rad}}_{u,0}$ represent the resonant excitation energy and decay linewidth, respectively. The first and second terms in the numerator correspond to the absorption and scattering forces, respectively. Note that the nonradiative decay width is a few millielectronvolts even at low temperatures (a few kelvin), whereas the radiative decay width is a few tens of microelectronvolts at most (see figure 11(a)). Therefore, the absorption force proportional to Γ in equation (99) dominates the dissipative force.

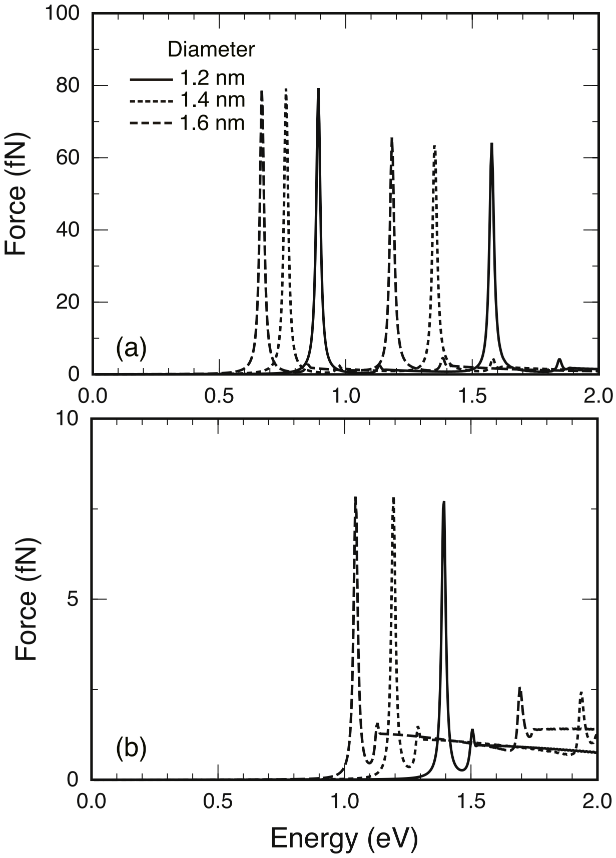

Figure 20. Calculated dissipative force for an EM field with (a) parallel and (b) perpendicular polarization. Effective strength of the Coulomb energy is set to $v = 0.15$. Reproduced with permission from [87]. Copyright 2009 American Physical Society.

Under resonant excitation ($\hbar\omega = \mathrm{Re}(\tilde{E}^0_u)$ in equation (99)), the dissipative force is given by

$$F^{\mathrm{res}}_Z \approx 4\kappa A I_0 \frac{1}{\varepsilon^0_u}\frac{\Gamma^{\mathrm{rad}}_{u,0}}{\Gamma + \Gamma^{\mathrm{rad}}_{u,0}}. \qquad (100)$$

Since Γ is much larger than $\Gamma^{\mathrm{rad}}_{u,0}$ even at low temperatures of a few kelvin, the resonant dissipative force is proportional to $1/\Gamma$. It increases monotonically with decreasing Γ and eventually reaches a maximum of $F^{\mathrm{res}}_Z = 4\kappa A I_0/\varepsilon^0_u$ at $\Gamma = 0$. The maximum dissipative force under resonant conditions is independent of the current density, i.e. oscillator strength. However, the linewidth $\Gamma^{\mathrm{rad}}_{u,0}$ of the radiation force is proportional to the oscillator strength; thus, the integrated force is proportional to the oscillator strength.

Figure 20 shows the dissipative force exerted on SWNTs with diameters of 1.2, 1.4 and 1.6 nm for (a) parallel and (b) perpendicular polarizations [87]. In this figure, we consider SWNTs with a length of 1 μm and an applied field intensity of $I_0 = 1$ MW cm^{-2}, which is comparable to that generally used in the optical tweezers [104]. The nonradiative decay width of $\hbar\Gamma = 10$ meV corresponds to the observed luminescence spectral width at room temperature [105–107]. Under resonant conditions, the force is 80 fN and the corresponding acceleration is 2.8×10^{7} m s^{-2}, where the mass density of a SWNT is 7.6×10^{-8} g cm^{-2}. This acceleration is much larger than that due to gravity.

For perpendicular polarization, the peak positions of the dissipative force differ from those for parallel polarization even when the SWNT has the same diameter because of the difference in the optical selection rules and the depolarization shift of a peak for perpendicular polarization. In addition, the depolarization effect suppresses the force peaks.

7.2. Gradient force

When the intensity of an EM field has a gradient at an object, a force is exerted on the object. To study the gradient force, we consider a standing plane wave consisting of counter-propagating plane waves: $\boldsymbol{D}(\boldsymbol{r}) = 2D\cos(qZ)\boldsymbol{e}$. We denote $B^{(0)}_{u,l}$ and $X_{u,l}$ for the standing wave by $B^{(0)\mathrm{st}}_{u,l}$ and $X^{\mathrm{st}}_{u,l}$, respectively. When a SWNT is located at position Z_0, $B^{(0)\mathrm{st}}_{u,l}$ is given by $2\cos(qZ_0)B^{(0)}_{u,l}$; thus, $X^{\mathrm{st}}_{u,l} = 2\cos(qZ_0)X_{u,l}$, where $B^{(0)}_{u,l}$ and $X_{u,l}$ are determined from the traveling wave $\boldsymbol{E}_0(\boldsymbol{r}) = E_0\mathrm{e}^{\mathrm{i}qZ}\boldsymbol{e}$. Substituting the above equations into equation (96), we obtain the following expression for the gradient force for the standing wave: [87]:

$$F_Z(\omega) = f(\omega)\sin(2qZ_0), \tag{101}$$

where

$$f(\omega) = -\frac{\hbar q}{\omega}\mathrm{Re}\left[\sum_u \frac{1}{\varepsilon^l_u} B^{(0)}_{u,l} X_{u,l}\right]. \tag{102}$$

In the individual exciton approximation, $f(\omega)$ for parallel polarization ($l = 0$) is written as

$$f(\omega) = -8\kappa A I_0 \sum_{u,l} \frac{\hbar\Gamma^{\mathrm{rad}}_{u,0}}{\varepsilon^0_u} \frac{\mathrm{Re}(\tilde{E}^0_u) - \hbar\omega}{[\mathrm{Re}(\tilde{E}^0_u) - \hbar\omega]^2 + (\hbar\Gamma + \hbar\Gamma^{\mathrm{rad}}_{u,0})^2}. \tag{103}$$

The gradient force as a function of the applied field frequency exhibits a dispersive lineshape, and the force is positive or negative depending on the applied field frequency.

The potential for the gradient force is represented by $U(\omega, Z_0) = f(\omega)[\cos(2qZ_0) - 1]/2q$. The minimum or maximum potentials lie at $Z_0 = \pi/(2q) + n\pi/q$ or $n\pi/q$, depending on the sign of $f(\omega)$, where n is an integer. The potential difference between the minimum and maximum is given by $\Delta U(\omega) = U[\omega, \pi/(2q)] - U(\omega, 0) = -f(\omega)/q$. For $f(\omega) > 0$ or $\Delta U(\omega) < 0$ (blue detuning), the potential minima lie at $Z_0 = \pi/(2q) + n\pi/q$, where the light intensity is zero. For $f(\omega) < 0$ or $\Delta U(\omega) > 0$ (red detuning), the potential minima lie at $Z_0 = n\pi/q$, where the light intensity is a maximum.

Figure 21 shows the potential $U(\omega_0, Z_0)$ for SWNTs with diameters of 1.2, 1.4 and 1.6 nm [87]. Each counter-propagating field intensity is $I_0 = 0.5$ MW cm^{-2} and the applied field frequency is fixed at $\hbar\omega_0 = 0.88$ eV. This frequency corresponds to resonant red detuning for a SWNT with $d = 1.2$ nm. The SWNT with $d = 1.2$ nm is strongly trapped at $Z_0 = 0$, which is the destabilization point for a SWNT with $d = 1.4$ nm. A SWNT with $d = 1.6$ nm experiences a small potential of approximately 10 meV, so it would move away from $Z_0 = 0$ at room temperature because of thermal fluctuations. Therefore, only the SWNT with $d = 1.2$ nm would be trapped. If we apply a stronger laser field such that the potential for the SWNT with $d = 1.6$ nm exceeds the thermal fluctuation energy, the SWNT with $d = 1.6$ nm is also trapped as well as that with $d = 1.2$ nm. Because the potential is proportional to the applied field intensity, we can estimate the appropriate laser field intensity for selective trapping of SWNTs having a specific structure. Furthermore, the potential for perpendicular polarization at this position is extremely small (see figure 21, inset). This indicates that we can trap SWNTs having a major axis oriented parallel to the light polarization.

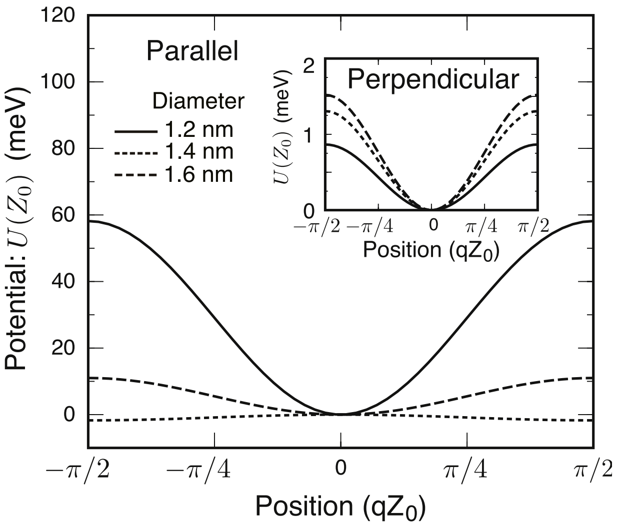

Figure 21. Calculated potential $U(Z_0)$ due to a gradient force for parallel polarization, shown as a function of SWNT position Z_0. Effective strength of the Coulomb energy is set to $v = 0.15$. Applied field frequency is $\hbar\omega_0 = 0.88$ eV, where a SWNT with $d = 1.2$ nm experiences red detuning. Inset shows the potential for perpendicular polarization. Reproduced with permission from [87]. Copyright 2009 American Physical Society.

A SWNT does not have a rigid structure in the axial direction under standard experimental conditions and is generally twisted in various directions. The above calculations are limited to a SWNT with a straight axis. To estimate the radiation force for the twisted SWNTs, we should calculate the statistical average of the force with respect to the axial direction. When the segments of a twisted SWNT have a completely random orientation, the averaged force is given by $F^{\mathrm{av}}_Z(\omega) = F^{\parallel}_Z(\omega)/2 + F^{\perp}_Z(\omega)/2$, where $F^{\parallel}_Z(\omega)$ and $F^{\perp}_Z(\omega)$ are the radiation force for parallel and perpendicular polarizations, respectively. The exciton levels for perpendicular polarization differ from those for parallel polarization and the force for perpendicular polarization is much smaller than that for parallel polarization. Therefore, it is feasible to consider the exciton resonance for parallel polarization in the selective manipulation and sorting of SWNTs. In the selected SWNTs, the major axis will be oriented parallel to the applied field polarization.

In experimental investigations of the radiation force exerted on SWNTs, a slight enrichment of semiconducting SWNTs was observed using an optical trap [108]. SWNTs with similar diameters were recently aggregated using a strongly focused laser beam [109]; several types of structures have been determined using resonant Raman spectra of the radial breathing modes. However, the analysis in this experiment was limited to the joint density of states calculated by using a simple tight-binding model. For more reliable identification of the structure of a SWNT, the exciton effect must be included in theoretical calculations. The exciton effect enhances the level separation due to warping and curvature [71]. A similar tendency has been calculated for the radiation force [87]. Therefore, by considering the excitonic effect, the resonant radiation force can be effectively used for manipulation and sorting of SWNTs having a specific structure, even when SWNTs have almost equal diameters.

8. Summary

The exciton states and optical properties of a SWNT have been discussed. The exciton states have been calculated from the screened Hartree–Fock approximation in the effective-mass or $\boldsymbol{k}\cdot\boldsymbol{p}$ scheme, which is quite useful for studying their essential global features. The exciton states of a SWNT have a large oscillator strength because SWNTs are a quasi-1D system; thus, absorption and PL can be observed even at room temperature. The optical properties, including the radiative lifetime of excitons, absorption spectra and radiation force, have been presented. These properties have been studied using a self-consistent treatment of EM fields and the induced current density appearing in the exciton–photon interaction. The resulting optical properties include the effect of the complex self-energy of the exciton. The imaginary part of the self-energy corresponds to the exciton's radiative decay width, which is fundamentally related to the scattering force. The self-consistent method provides a unified treatment of these optical properties. In addition, a dynamical e–h EXI can be derived from the self-consistent treatment. In contrast to the conventional e–h EXI, the dynamical EXI includes a dynamical factor, which plays an important role for excitons having a large oscillator strength, such as SWNT excitons. In fact, the absorption of a SWNT calculated using the dynamical e–h EXI, which agrees with that calculated including the depolarization effect, differ significantly from those calculated using the conventional e–h EXI.

A SWNT exhibits various optical properties because of its peculiar cylindrical shape, massless Dirac fermions, and the existence of K and K′ valleys. The optical selection rules depend on the direction of the applied field polarization. The optical absorption, radiation force and radiative lifetime of excitons for perpendicular polarization are significantly suppressed by the depolarization effect or e–h EXI. Singlet excitons are classified as having bright even-parity and dark odd-parity states; this is a typical feature of excitons in a quasi-1D system. There exists a new type of dark $^1|\mathrm{KK}-\mathrm{K'K'}(-)\rangle$ and bright $^1|\mathrm{KK}-\mathrm{K'K'}(-)\rangle$ states consisting of even-parity excitons in the K and K′ valleys, respectively. By applying a magnetic flux passing through the cross section of a SWNT, these two excitons can be split symmetrically by increasing the magnetic flux. In this situation, these two excitons approach to $^1|\mathrm{KK}\rangle$ and $^1|\mathrm{K'K'}\rangle$ bright excitons because the degeneracy of $^1|\mathrm{KK}\rangle$ and $^1|\mathrm{K'K'}\rangle$ is lifted due to the AB effect. Level separation between $^1|\mathrm{KK}-\mathrm{K'K'}(+)\rangle$ and $^1|\mathrm{KK}-\mathrm{K'K'}(-)\rangle$ excitons in the absence of a magnetic field has been measured in absorption spectra taken under high magnetic fields. For perpendicular polarization, $^1|\mathrm{KK}-\mathrm{K'K'}(-)\rangle$ has a smaller oscillator strength, in contrast to the dark exciton $^1|\mathrm{KK}-\mathrm{K'K'}(-)\rangle$ for parallel polarization. This $^1|\mathrm{KK}-\mathrm{K'K'}(-)\rangle$ state is considered a quasi-dark exciton. Its existence is attributed to the small level separation between $^1|\mathrm{KK}\rangle$ and $^1|\mathrm{K'K'}\rangle$ due to the e–h band anisotropy.

Acknowledgments

The author acknowledges the theoretical collaboration with Professors Ando, Cho, Ishihara, Uryu, Dr Iida and Mr Ishikawa. The author also thanks Professors Kono, Miyauchi, and Maruyama for fruitful experimental and theoretical collaboration. This work was supported in part by a Grant-in-Aid for Scientific Research on the Priority Area 'Carbon Nanotube Nanoelectronics' from the Ministry of Education, Culture, Sports, Science and Technology Japan.

References

[1] Iijima S 1991 *Nature* **354** 56
[2] Oberlin A, Endo M and Koyama T 1976 *J. Cryst. Growth* **32** 335
[3] Iijima S and Ichihashi T 1993 *Nature* **363** 603
[4] Bethune D S, Klang C H, De Vries M S, Gorman G, Savoy R, Vazquez J and Beyers R 1993 *Nature* **363** 605
[5] Hamada N, Sawada S and Oshiyama A 1992 *Phys. Rev. Lett.* **68** 1579
[6] Mintmire J W, Dunlap B I and White C T 1992 *Phys. Rev. Lett.* **68** 631
[7] Dresselhaus M S, Dresselhaus G and Saito R 1992 *Phys. Rev.* B **45** 6234
[8] Saito R, Fujita M, Dresselhaus G and Dresselhaus M S 1992 *Phys. Rev.* B **46** 1804
[9] Tanaka K, Okahara K, Okada M and Yamabe T 1992 *Chem. Phys. Lett.* **191** 469
[10] Ajiki H and Ando T 1993 *J. Phys. Soc. Japan* **62** 1255
[11] Bachilo S M, Strano M S, Kittrell C, Hauge R H, Smalley R E and Weisman R B 2002 *Science* **298** 2361
[12] Hagen A and Hertel T 2003 *Nano Lett.* **3** 383
[13] Jorio A *et al* 2005 *Phys. Rev.* B **71** 075401
[14] Ajiki H and Ando T 1994 *Physica* B **201** 349
[15] Duesberg G S, Loa I, Burghard M, Syassen K and Roth S 2000 *Phys. Rev. Lett.* **85** 5436
[16] Jorio A *et al* 2002 *Phys. Rev.* B **65** 121402
[17] Hartschuh A, Pedrosa H N, Novotny L and Krauss T D 2003 *Science* **301** 1354
[18] Hwang J, Gommans H H, Ugawa A, Tashiro H, Haggenmueller R, Winey K I, Fischer J E, Tanner D B and Rinzler A G 2000 *Phys. Rev.* B **62** 13310
[19] Islam M F, Milkie D E, Kane C L, Yodh A G and Kikkawa J M 2004 *Phys. Rev. Lett.* **93** 37404

[20] Zaric S, Ostojic G N, Kono J, Shaver J, Moore V C, Hauge R H, Smalley R E and Wei X 2004 *Nano Lett.* **4** 2219

[21] Islam M F, Milkie D E, Torrens O N, Yodh A G and Kikkawa J M 2005 *Phys. Rev.* B **71** 201401

[22] Torrens O N, Milkie D E, Ban H Y, Zheng M, Onoa G B, Gierke T D and Kikkawa J M 2007 *J. Am. Chem. Soc.* **129** 252

[23] Searles T A, Imanaka Y, Takamasu T, Ajiki H, Fagan J A, Hobbie E K and Kono J 2010 *Phys. Rev. Lett.* **105** 17403

[24] Ajiki H and Ando T 1993 *J. Phys. Soc. Japan* **62** 2470

[25] Lu J P 1995 *Phys. Rev. Lett.* **74** 1123

[26] Ajiki H and Ando T 1995 *J. Phys. Soc. Japan* **64** 4382

[27] Zaric S, Ostojic G N, Kono J, Shaver J, Moore V C, Strano M S, Hauge R H, Smalley R E and Wei X 2004 *Science* **304** 1129

[28] Zaric S *et al* 2006 *Phys. Rev. Lett.* **96** 16406

[29] Matsunaga R, Matsuda K and Kanemitsu Y 2008 *Phys. Rev. Lett.* **101** 147404

[30] Takeyama S, Suzuki H, Yokoi H, Murakami Y and Maruyama S 2011 *Phys. Rev.* B **83** 235405

[31] Kataura H, Kumazawa Y, Maniwa Y, Umezu I, Suzuki S, Ohtsuka Y and Achiba Y 1999 *Synth. Met.* **103** 2555

[32] Jost O *et al* 1999 *Appl. Phys. Lett.* **75** 2217

[33] Ichida M, Mizuno S, Tani Y, Saito Y and Nakamura A 1999 *J. Phys. Soc. Japan* **68** 3131

[34] O'Connell M J *et al* 2002 *Science* **297** 593

[35] Lefebvre J, Fraser J M, Finnie P and Homma Y 2004 *Phys. Rev.* B **69** 075403

[36] Mann D, Kato Y K, Kinkhabwala A, Pop E, Cao J, Wang X, Zhang L, Wang Q, Guo J and Dai H 2007 *Nature Nanotechnol.* **2** 33

[37] Son H, Hori Y, Chou S G, Nezich D, Samsonidze G G, Dresselhaus G, Dresselhaus M S and Barros E B 2004 *Appl. Phys. Lett.* **85** 4744

[38] Tsyboulski D A, Bachilo S M and Weisman R B 2005 *Nano Lett.* **5** 975

[39] Ohno Y, Iwasaki S, Murakami Y, Kishimoto S, Maruyama S and Mizutani T 2006 *Phys. Rev.* B **73** 235427

[40] Ando T 2010 *J. Phys. Soc. Japan* **79** 024706

[41] Moritsubo S, Murai T, Shimada T, Murakami Y, Chiashi S, Maruyama S and Kato Y K 2010 *Phys. Rev. Lett.* **104** 247402

[42] Dresselhaus M S, Dresselhaus G, Jorio A, Souza Filho A G and Saito R 2002 *Carbon* **40** 2043

[43] Dresselhaus M S, Dresselhaus G, Saito R and Jorio A 2005 *Phys. Rep.* **409** 47

[44] Jorio A, Dresselhaus G and Dresselhaus M S (ed) 2008 *Carbon Nanotubes: Advanced Topics in the Synthesis, Structure, Properties and Applications* vol 111 (Berlin: Springer)

[45] Jorio A, Dresselhaus M S, Saito R and Dresselhaus G 2011 *Raman Spectroscopy in Graphene Related Systems* (Weinheim: Wiley–VCH)

[46] Dresselhaus M S, Dresselhaus G and Eklund P C 1996 *Science of Fullerenes and Carbon Nanotubes* (San Diego, CA: Academic)

[47] Ajiki H and Ando T 1997 *Solid State Commun.* **102** 135

[48] Saito R, Dresselhaus G and Dresselhaus M S 1998 *Physical Properties of Carbon Nanotubes* (London: Imperial College Press)

[49] Ando T 2000 *Semicond. Sci. Technol.* **15** R13

[50] Dresselhaus M S, Dresselhaus G and Avouris P (ed) 2000 *Carbon Nanotubes: Synthesis, Structure, Properties and Applications* (Berlin: Springer)

[51] Dresselhaus M S and Eklund P C 2000 *Adv. Phys.* **49** 705

[52] Harris P J F, Hernández E and Yakobson B I 2004 *Am. J. Phys.* **72** 415

[53] Reich S, Thomsen C and Maultzsch J 2004 *Carbon Nanotubes: Basic Concepts and Physical Properties* (Weinheim: Wiley–VCH)

[54] Ando T 2005 *J. Phys. Soc. Japan* **74** 777

[55] Charlier J C, Blase X and Roche S 2007 *Rev. Mod. Phys.* **79** 677

[56] Brand O, Fedder G K, Hierold C, Korvink J G and Tabata O (ed) 2008 *Carbon Nanotube Devices: Properties, Modeling, Integration and Applications* (Weinheim: Wiley–VCH)

[57] Saito S and Zettl A (ed) 2008 *Carbon Nanotubes: Quantum Cylinders of Graphene* (Amsterdam: Elsevier)

[58] Guldi D M and Martin N 2010 *Carbon Nanotubes and Related Structures: Synthesis, Characterization, Functionalization, and Applications* (Weinheim: VCH–Wiley)

[59] Ajiki H and Ando T 1996 *J. Phys. Soc. Japan* **65** 505

[60] Ando T 2004 *J. Phys. Soc. Japan* **73** 3351

[61] Kane C L and Mele E J 1997 *Phys. Rev. Lett.* **78** 1932

[62] Ando T 2000 *J. Phys. Soc. Japan* **69** 1757

[63] Weisman R B and Bachilo S M 2003 *Nano Lett.* **3** 1235

[64] Fantini C, Jorio A, Souza M, Strano M S, Dresselhaus M S and Pimenta M A 2004 *Phys. Rev. Lett.* **93** 147406

[65] Sato K, Saito R, Jiang J, Dresselhaus G and Dresselhaus M S 2007 *Phys. Rev.* B **76** 195446

[66] Ando T 2009 *J. Phys. Soc. Japan* **78** 104703

[67] Grüneis A, Saito R, Jiang J, Samsonidze G G, Pimenta M A, Jorio A, Souza Filho A G, Dresselhaus G and Dresselhaus M S 2004 *Chem. Phys. Lett.* **387** 301

[68] Ando T 1997 *J. Phys. Soc. Japan* **66** 1066

[69] Spataru C D, Ismail-Beigi S, Benedict L X and Louie S G 2004 *Phys. Rev. Lett.* **92** 77402

[70] Chang E, Bussi G, Ruini A and Molinari E 2004 *Phys. Rev. Lett.* **92** 196401

[71] Jiang J, Saito R, Samsonidze G G, Jorio A, Chou S G, Dresselhaus G and Dresselhaus M S 2007 *Phys. Rev.* B **75** 035407

[72] Ichida M, Mizuno S, Saito Y, Kataura H, Achiba Y and Nakamura A 2002 *Phys. Rev.* B **65** 241407

[73] Kane C L and Mele E J 2003 *Phys. Rev. Lett.* **90** 207401

[74] Wang F, Dukovic G, Brus L E and Heinz T F 2005 *Science* **308** 838

[75] Maultzsch J, Pomraenke R, Reich S, Chang E, Prezzi D, Ruini A, Molinari E, Strano M S, Thomsen C and Lienau C 2005 *Phys. Rev.* B **72** 241402

[76] Ogawa T and Takagahara T 1991 *Phys. Rev.* B **44** 8138

[77] Uryu S, Ajiki H and Ando T 2008 *Phys. Rev.* B **78** 115414

[78] Ajiki H 2012 *J. Phys. Soc. Jpn.* submitted

[79] Sham L J and Rice T M 1966 *Phys. Rev.* **144** 708

[80] Heller W R and Marcus A 1951 *Phys. Rev.* **84** 809

[81] Onodera Y and Toyozawa Y 1967 *J. Phys. Soc. Japan* **22** 833

[82] Toyozawa Y 1980 *The Physics of Elementary Excitations* (Berlin: Springer) chapter 2

[83] Cho K 2003 *Optical Response of Nanostructures: Microscopic Nonlocal Theory* (Berlin: Springer) chapter 1

[84] Ando T 2006 *J. Phys. Soc. Japan* **75** 024707

[85] Miyauchi Y, Ajiki H and Maruyama S 2010 *Phys. Rev.* B **81** 121415

[86] Uryu S and Ando T 2006 *Phys. Rev.* B **74** 155411

[87] Ajiki H, Iida T, Ishikawa T, Uryu S and Ishihara H 2009 *Phys. Rev.* B **80** 115437

[88] Cho K 1991 *Prog. Theor. Phys. Suppl.* **106** 225

[89] Ajiki H, Tsuji T, Kawano K and Cho K 2002 *Phys. Rev.* B **66** 245322

[90] Chew W 1995 *Waves and Fields in Inhomogeneous Media* (Piscataway, NJ: IEEE)

[91] Spataru C D, Ismail-Beigi S, Capaz R B and Louie S G 2005 *Phys. Rev. Lett.* **95** 247402

[92] Citrin D S 1992 *Phys. Rev. Lett.* **69** 3393

[93] Hagen A, Moos G, Talalaev V and Hertel T 2004 *Appl. Phys.* A **78** 1137

[94] Chen W 1976 *Surf. Sci.* **58** 263

[95] Allen S J, Tsui D C and Vinter B 1976 *Solid State Commun.* **20** 425

[96] Ando T 1977 *Z. Phys.* B **26** 263

[97] Kindo K, Takeyama S, Tokunaga M, Matsuda Y H, Kojima E, Matsuo A, Kawaguchi K and Sawabe H 2010 *J. Low Temp. Phys.* **159** 381

[98] Shaver J, Kono J, Portugall O, Krstic V, Rikken G L J A, Miyauchi Y, Maruyama S and Perebeinos V 2007 *Nano Lett.* **7** 1851

[99] Uryu S and Ando T 2011 *Phys. Rev.* B **83** 085404

[100] Iida T and Ishihara H 2003 *Phys. Rev. Lett.* **90** 57403

[101] Iida T and Ishihara H 2008 *Phys. Rev.* B **77** 245319

[102] Iida T and Ishihara H 2006 *Phys. Rev. Lett.* **97** 117402

[103] Ashkin A, Dziedzic J M, Bjorkholm J E and Chu S 1986 *Opt. Lett.* **11** 288

[104] Guntherodt H J, Anselmetti D and Meyer E 1995 *Forces in Scanning Probe Methods* (*NATO ASI Series*) (Dordrecht: Kluwer Academic)

[105] Inoue T, Matsuda K, Murakami Y, Maruyama S and Kanemitsu Y 2006 *Phys. Rev.* B **73** 233401

[106] Matsuda K, Inoue T, Murakami Y, Maruyama S and Kanemitsu Y 2008 *Phys. Rev.* B **77** 033406

[107] Ichida M, Kiyohara Y, Saito S, Miyata Y, Kataura H and Ando H 2008 *Phys. Status Solidi* b **245** 2712

[108] Tan S, Lopez H A, Cai C W and Zhang Y 2004 *Nano Lett.* **4** 1415

[109] Rodgers T, Shoji S, Sekkat Z and Kawata S 2008 *Phys. Rev. Lett.* **101** 127402